IAHR AIRH

Journal of Hydraulic Research Vol. 48 Extra Issue (2010), pp. 6–27
doi:10.3826/jhr.2010.0012

State-of-the-art of classical SPH for free-surface flows

Etat de l'art de la méthode SPH pour les écoulements à surface libre

MONCHO GOMEZ-GESTEIRA, *EPHYSLAB (Environmental Physics Laboratory), University of Vigo, Spain (author for correspondence)*

BENEDICT D. ROGERS, *School of Mechanical, Aerospace and Civil Engineering, University of Manchester, UK*

ROBERT A. DALRYMPLE, *Department of Civil Engineering, Johns Hopkins University, Baltimore, MD 21218, USA*

ALEX J.C. CRESPO, *EPHYSLAB (Environmental Physics Laboratory), University of Vigo, Spain; School of Mechanical, Aerospace and Civil Engineering, University of Manchester, UK*

ABSTRACT
Smoothed Particle Hydrodynamics (SPH) is the most widely established mesh-free method which has been used in several fields as astrophysics, solids mechanics and fluid dynamics. In the particular case of computational fluid dynamics, the model is beginning to reach a maturity that allows carrying out detailed quantitative comparisons with laboratory experiments. Here the state-of-the-art of the classical SPH formulation for free-surface flow problems is described in detail. This is demonstrated using dam-break simulations in 2-D and 3-D. The foundations of the method will be presented using different derivations based on the method of interpolants and on the moving least-squares approach. Different methods to improve the classic SPH approach such as the use of density filters and the corrections of the kernel function and its gradient are examined and tested on some laboratory cases.

RÉSUMÉ
La méthode SPH est la méthode numérique sans maillage la plus largement établie et utilisée en astrophysique, mécanique des solides et dynamique des fluides. Dans le cas particulier de la simulation numérique des écoulements, le modèle commence à atteindre une maturité suffisante pour permettre des comparaisons quantitatives détaillées avec des mesures expérimentales. Dans cet article, l'état de l'art de la formulation SPH classique pour les problèmes d'écoulements à surface libre est décrit en détail, en s'appuyant sur des simulations de rupture de barrage en 2D et 3D. Les fondements de la méthode sont présentés selon différentes approches basées sur la méthode des interpolateurs et sur les moindres carrés mobiles. Différentes méthodes d'amélioration de l'approche SPH classique telles que l'utilisation de filtrage de la densité et les techniques de correction de la fonction noyau et de son gradient sont examinées et testées sur des cas de laboratoire.

Keywords: Computational fluids, dam break, density correction, kernel correction, smoothed particle hydrodynamics, SPH

1 Introduction

Computational fluid dynamics (CFD) provides an alternative and valuable tool of scientific investigation. On the one hand CFD permits carrying out numerical experiments instead of expensive and, in some cases, impossible experiments, where similarity principles cannot be invoked and scale models cannot be used. On the other hand, CFD provides additional information that cannot be obtained from direct experimental observation, which is especially valuable when the aim of the study is not only to describe some flow variable (such as velocity, pressure, etc.) but understanding the physical processes controlling the phenomenon (Liu and Losada 2002).

Historically, CFD has focused on grid-based methods, where two different frames are usually considered for describing the physical governing equations, namely; the Eulerian and the Lagrangian description. The finite element method element method (FEM) is the paradigm of Lagrangian methods, where a grid is attached on the material and it can deform, to a certain extent, following the deformation of the material. The Eulerian description is commonly represented by the finite difference method (FDM) and the finite volume method (FVM), which are the dominant methods in CFD. In spite of the doubtless successes obtained during the last decades, both Eulerian and Lagrangian approaches present important limitations, even when used in a combined way (Hans 1999, Belytschko *et al.* 2000).

The use of mesh-free methods for CFD has experienced an exponential growing during the last decade (for a complete description see Liu (2003) and Belytschko *et al.* (1996)). These methods, whose main idea is to substitute the grid by a set of arbitrarily distributed nodes, are expected to be more adaptable and versatile than the conventional grid-based methods, especially for those applications with severe discontinuities in the fluid.

Smoothed Particle Hydrodynamics (SPH), which was invented in 1977 for simulating astrophysical problems (Lucy 1977, Gingold and Monaghan 1977), is arguably the most popular

Revision received March 1, 2009/Open for discussion until June 30, 2010.

mesh-free method. Conceptually, the method uses integral interpolation theory and transforms the partial differential equations into an integral form (reviews and background of the methodology are provided by Monaghan 1992, Monaghan 2005, Liu and Liu 2003). In spite of its early appearance, the method did not attract the interest of researchers in other fields until the beginning of the 1990s, when the method was successfully applied in fields such as impact penetration in solids (Libersky *et al.* 1993, Randles and Libersky 1996) and two-phase flow (Monaghan 1997).

In the particular case of fluid dynamics, perhaps the most important success of the meshless SPH technique has been the application of the method to free-surface flows, first attempted by Monaghan (1994). Monaghan also studied the behavior of gravity currents and solitary waves (Monaghan 1996, Monaghan *et al.* 1999), the wave arrival at a beach (Monaghan and Koss 1999) or the behavior of a Scott Russell's wave generator (Monaghan and Kos 2000). In addition, Morris *et al.* (1997) introduced an improved second-order derivative formulation to treat viscosity and study low Reynolds incompressible flows. Other authors (Shao and Lo 2003) studied the wave mechanics by means of an incompressible SPH, in particular the model was applied to the study of the wave-breakwater interaction (Gotoh *et al.* 2004, Shao 2005). The same authors also analyzed the behavior of breaking waves (Shao 2006). Also at the beginning of the 2000s, Colagrossi and Landrini (2003) considered the study of interfacial flows and introduced the use of density filters. The *Electricite de France* (EDF) group has successfully used their code to study both incompressible flows (Issa *et al.* 2005, Lee *et al.* 2008) and turbulent free-surface flows (Violeau and Issa 2007). The SPHysics group (http://www.sphysics.org) has mainly focused its research on the wave propagation and interaction with coastal structures, both in 2D (Gomez-Gesteira *et al.* 2005, Dalrymple and Rogers 2006, Crespo *et al.* 2007a) and 3D (Gomez-Gesteira and Dalrymple 2004, Crespo *et al.* 2007b, Crespo *et al.* 2008). Other authors have focused their interest on the study of sloshing type problems (Souto-Iglesias *et al.* 2004, Souto-Iglesias *et al.* 2006, Delorme *et al.* 2008), the interaction of solids with liquid (Oger *et al.* 2006) simulating wedge water entries, the simulation of flows in Pelton turbines (Marongiu *et al.* 2007) or near shore processes (Landrini *et al.* 2007). Some multiphase work for free-surface flows has been attempted with limited success (Colagrossi and Landrini 2003, Cuomo *et al.* 2006). However, part of the success of the SPH technique can be attributed to the good results obtained by the aforementioned work for modeling free-surface fluid flows using solely a single-phase approach.

As the most widely used formulation to date, the aim of this paper is to describe the background of classical SPH and its application to free-surface flows (alternative formulations can be seen in the literature: Vila (1999), Ferrari *et al.* (2009), Molteni *et al.* (2007), Colagrossi and Landrini (2003)). Special attention will be paid to the capabilities of the method to solve free-surface problems in general and wave problems in particular. Different improvements and refinements of the classical technique will also be analyzed. The SPHysics model will be used to depict the different parameterizations considered to analyze dambreak problems (Nsom *et al.* 2000, Chanson 2009), which constitute a well suited benchmark for SPH method.

2 Smoothed Particle Hydrodynamics: Theoretical background

2.1 *Introduction*

In SPH, the fluid domain is represented by a set of irregularly spaced nodal points where physical properties (e.g., mass, density, velocity, position, pressure) are known. These nodal points then move with the fluid hence making the technique a Lagrangian meshless method. These properties can change with time due to the interactions with neighboring particles.

2.2 *Derivation from interpolation method*

The SPH method is based on the following integral

$$f(\mathbf{s}, t) = \int_v W(\mathbf{s} - \mathbf{x}, h)\, f(\mathbf{x}, t) dv \tag{1}$$

where the integral is over the domain v and dv is the element of volume which depends on the dimensionality of the problem and $W(\mathbf{s}-\mathbf{x}, h)$ is the weighting function also called *smoothing kernel* in SPH. The size of the kernel is determined by the parameter h, which determines a domain of influence around $\mathbf{s}$. In 3D that domain is a sphere of radius nh, where n depends on the kernel definition. Although h is a constant in the simplest applications of SPH, the parameter can depend both on time and space as described in Monaghan (1992).

For computational purposes, the integrals are approximated numerically by a summation of contributions from the surrounding particles in the domain:

$$f(\mathbf{s}, t) \approx \sum_j W(\mathbf{s} - \mathbf{x}_j, h)\, f_j \Delta v_j \tag{2}$$

such that

$$\sum_j W(\mathbf{s} - \mathbf{x}_j, h) \Delta v_j = 1 \tag{3}$$

where Δv_j is the volume associated with particle j. In SPH the mass, m_j, of particle j remains fixed and the density, ρ_j, is allowed to vary. Note that in the classical SPH formulation, when solving the Navier-Stokes equations the fluid is treated as compressible. If water is being simulated, then an artificial equation of state is used (Monaghan 1994); alternatively some authors have considered incompressible formulations solving a pressure-Poisson equation (Shao and Lo 2003, Gotoh *et al.* 2004, Shao 2005, Lee *et al.* 2008). In general, the volume is replaced by $\Delta v_j = m_j/\rho_j$ in such a way that Eq. (2) becomes

$$f(\mathbf{s}, t) \approx \sum_j \frac{m_j}{\rho_j} W(\mathbf{s} - \mathbf{x}_j, h)\, f_j \tag{4}$$

2.3 *Moving Least-Squares interpolant*

An alternative approach to derive SPH is using a moving least-square (MLS) approximation (Belytschko *et al.* 1996, Dilts

1999), described recently in Dalrymple *et al.* (2009). Given a set of irregularly spaced data denoted $f(\mathbf{x}_i)$ for $i = 1, \ldots, N$, the interpolating function at any value of $\mathbf{s}$ is

$$f_p(\mathbf{s}) = \sum_j^M a_j(\mathbf{s}) p_j(\mathbf{s}) \equiv \mathbf{p}^{\mathrm{T}}(\mathbf{s})\mathbf{a}(\mathbf{s}) \tag{5}$$

where $\mathbf{p}^{\mathrm{T}}(\mathbf{s})$ are monomials in the coordinate $\mathbf{s}$ and $M < N$. For example, in two dimensions, the linear and quadratic bases are $\mathbf{p}^{\mathrm{T}}(\mathbf{s}) = [1, x, y]$ with $M = 3$ and $\mathbf{p}^{\mathrm{T}}(\mathbf{s}) = [1, x, y, x^2, xy, y^2]$ with $M = 6$.

The coefficients of the interpolating function, $\mathbf{a}(\mathbf{s})$, vary with location, hence the name "*moving*". To find these coefficients at position $\mathbf{s}$, the sum of the weighted squared errors between the interpolating function for each position $\mathbf{x}_i$ and data f_i is computed:

$$\mathrm{Err}(\mathbf{s}) = \sum_{i=1}^N W(\mathbf{s} - \mathbf{x}_i)(\mathbf{p}^{\mathrm{T}}(\mathbf{x}_i)\mathbf{a}(\mathbf{s}) - f_i)^2 \tag{6}$$

where $W(\mathbf{s} - \mathbf{x}_i)$ is a weighting function for node i that decays with the distance from the node to position $\mathbf{s}$. Coefficients $\mathbf{a}(\mathbf{s})$ are calculated by minimizing the mean-squared error with respect to those coefficients.

$$\frac{\partial E}{\partial \mathbf{a}} = \mathbf{A}(\mathbf{s})\mathbf{a}(\mathbf{s}) - \mathbf{B}(\mathbf{s})\mathbf{f} = 0 \tag{7}$$

where

$$\mathbf{f}^{\mathrm{T}} = (f_1, f_2, \ldots, f_N) \tag{8}$$

$$P = \begin{bmatrix} p_1(\mathbf{x}_1) & p_2(\mathbf{x}_1) & \cdots & p_M(\mathbf{x}_1) \\ p_1(\mathbf{x}_2) & p_2(\mathbf{x}_2) & \cdots & p_M(\mathbf{x}_2) \\ \vdots & \vdots & \vdots & \vdots \\ p_1(\mathbf{x}_N) & p_2(\mathbf{x}_N) & \cdots & p_M(\mathbf{x}_N) \end{bmatrix} \tag{9}$$

$$W(\mathbf{s}) = \begin{bmatrix} W(\mathbf{s} - \mathbf{x}_1) & 0 & \cdots & 0 \\ 0 & W(\mathbf{s} - \mathbf{x}_2) & \cdots & 0 \\ \vdots & \vdots & \vdots & \vdots \\ 0 & 0 & \cdots & W(\mathbf{s} - \mathbf{x}_N) \end{bmatrix} \tag{10}$$

Solving, $\mathbf{a}(\mathbf{s}) = \mathbf{A}^{-1}(\mathbf{s})\mathbf{B}(\mathbf{s})\mathbf{f}$ the local approximation at $\mathbf{s}$ is then given by Eq. (5).

The simplest interpolation is based on using only the first constant monomial, which is simply fitting a constant locally; this results in

$$a = \frac{\sum_j W(\mathbf{s} - \mathbf{x}_j, h) f_j}{\sum_j W(\mathbf{s} - \mathbf{x}_j, h)} \tag{11}$$

and, consequently,

$$f(\mathbf{s}, t) = \sum_j \frac{W(\mathbf{s} - \mathbf{x}_j, h)}{\sum_k W(\mathbf{s} - \mathbf{x}_k, h)} f_j(t) \tag{12}$$

which is usually known as the Shepard interpolant. More sophisticated local fitting involves linear or higher order monomials which results in the use of matrix inversions for the fitting, e.g., Colagrossi and Landrini (2003).

2.4 *Kernels*

According to Monaghan (1982), the kernel is required to satisfy the following conditions

$$W(\mathbf{s} - \mathbf{x}, h)\rangle 0 \quad \text{over the domain } v. \tag{13.1}$$

$$W(\mathbf{s} - \mathbf{x}, h) = 0 \quad \text{outside the domain } v. \tag{13.2}$$

$$\int_v W(\mathbf{s} - \mathbf{x}, h)dv = 1 \quad \text{(partition of unity).} \tag{13.3}$$

$W(q, h)$ decreases monotonically with distance

$$q = \|s - x\|/h. \tag{13.4}$$

$$W(q, h) \to \delta(q) \quad \text{when } h \to 0, \quad \text{being } \delta \text{ a delta function.} \tag{13.5}$$

According to Belytschko *et al.* (1996) the last condition is unnecessary since any realistic function with compact support and satisfying the four first conditions approaches a delta function. In addition, the limit $h \to 0$ is never reached in real computations.

There are a variety of possible weighting functions (see Liu and Liu (2003) for a complete description). Gingold and Monaghan (1977) use a Gaussian kernel, which is considered to be the first "golden rule" of SPH (Monaghan 1992). Nevertheless, this kernel is C^{-1}, since it is not equal to zero at any finite distance as pointed out by Belytschko *et al.* (1996). A renormalized Gaussian kernel with a cut-off limit ($3h$) to match the third property is used in (Colagrossi and Landrini 2003, Landrini *et al.* 2007, Delorme *et al.* 2008). Dalrymple and Rogers (2006) use a quadratic kernel previously defined by Johnson *et al.* (1996), which has no inflection in its first derivative, in such a way that the force between particles increases continuously when decreasing the inter-particle spacing. For the propagation of nonlinear waves, Rogers and Dalrymple (2008) demonstrated that using a quadratic kernel and its linear gradient still preserves the nonlinear free-surface wave properties. Possibly, the most commonly used kernel is the cubic-spline kernel (see, for example, Monaghan and Kos 1999, Gomez-Gesteira and Dalrymple 2004, Souto-Iglesias *et al.* 2004, Shao 2005, Gomez-Gesteira *et al.* 2005, Souto-Iglesias *et al.* 2006, Crespo *et al.* 2007b, Crespo *et al.* 2008)). Other authors prefer higher order kernels, as the fourth-order spline used by Violeau and Issa (2007). The kernel used in the Moving Particle Semi-implicit method (MPS) (Koshizuka *et al.* 1995) depends on q^{-1}, in such a way that both the kernel and its first derivative, which is proportional to the force in Navier-Stokes equation (to be shown later), diverge when the inter-particle space tends to zero. In general, the accuracy of the SPH interpolation increases with the order of the polynomial used in the weighting function (Capone *et al.* 2007). However, the computational time also increases with the order of the kernels. The quintic kernel used by Lucy (1977) and Wendland (1995) can constitute a good choice since it provides a higher order of interpolation with a computational cost comparable to the quadratic kernel.

2.5 *Derivatives*

One of the main advantages of SPH is that a differentiable interpolant of any function can be constructed from its values at the particles simply by using a differentiable kernel in the summation process. So, given a scalar function A, its gradient can be calculated as

$$\nabla A_i(\mathbf{s}, t) = \sum_j \frac{m_j}{\rho_j} \nabla W(\mathbf{s} - \mathbf{x}_j, h) A_j \tag{14}$$

But, following Monaghan's second golden rule of SPH (Monaghan 1992) the density should be placed inside operator. So, using

$$\rho \nabla A = \nabla(\rho A) - A \nabla \rho \tag{15}$$

the gradient of A at particle i can be calculated from

$$\nabla A_i(\mathbf{s}, t) = \sum_j \frac{m_j}{\rho_j} (A_j - A_i) \nabla W(\mathbf{s} - \mathbf{x}_j, h) \tag{16}$$

A similar expression can be used to calculate the divergence of any vectorial function (e.g. velocity).

$$\mathrm{div}(\mathbf{u}_i) = \sum_j \frac{m_j}{\rho_j} (\mathbf{u}_j - \mathbf{u}_i) \nabla W(\mathbf{s} - \mathbf{x}_j, h) \tag{17}$$

2.6 *SPH improvements*

The SPH discrete summation procedure can generate important inaccuracies in the vicinity of the boundaries and close to free-surfaces, where the normalization condition is not fulfilled. Considerable effort has been devoted to overcome this problem, which has mainly concentrated on approaches that either corrects the kernel and/or its first derivative, or by performing density filters, which can help to stabilize the pressure field. Note that for the sake of clarity the kernel will be denoted W_{ij} instead of $W(\mathbf{s} - \mathbf{x}_j, h)$ from now on when used in discrete notation.

2.6.1 *Density filters*

While the kinematics of SPH simulations is generally realistic, the pressure field of the particles can exhibit large pressure oscillations, which can be particularly important in the near boundary areas and close to free-surfaces. One of the most straightforward and computationally least expensive methods to smooth out pressure oscillations is to perform a filter over the density of the particles and to re-assign a density to each particle as done by Colagrossi and Landrini (2003) following Belytschko *et al.* (1998) and Dilts (1999). Two orders of correction are usually considered.

2.6.1.1 Zeroth order – Shepard filter

The Shepard filter is a quick and simple correction to the density field, and the following procedure is applied every m (= 20–50) time steps

$$\rho_i^{\mathrm{new}} = \sum_j \rho_j \tilde{W}_{ij} \frac{m_j}{\rho_j} = \sum_j m_j \tilde{W}_{ij} \tag{18}$$

where the kernel has been corrected using a zeroth-order correction:

$$\tilde{W}_{ij} = \frac{W_{ij}}{\sum_j W_{ij} \frac{m_j}{\rho_j}} \tag{19}$$

First order – Moving Least Squares (MLS) The Moving Least Squares (MLS) approach was developed by Dilts (1999) and applied by Colagrossi and Landrini (2003). The method is a first-order correction so that the linear variation of the density field can be exactly reproduced:

$$\rho_i^{\mathrm{new}} = \sum_j \rho_j W_{ij}^{\mathrm{MLS}} \frac{m_j}{\rho_j} = \sum_j m_j W_{ij}^{\mathrm{MLS}} \tag{20}$$

The corrected kernel is evaluated as follows:

$$W_{ij}^{\mathrm{MLS}} = \beta(\mathbf{x}_i) \cdot (\mathbf{x}_i - \mathbf{x}_j) W_{ij} \tag{21}$$

so that, for example, in 2-D

$$W_{ij}^{\mathrm{MLS}} = [\beta_0(\mathbf{x}_i) + \beta_{1x}(\mathbf{x}_i)(x_i - x_j) + \beta_{1z}(\mathbf{x}_i)(z_i - z_j)] W_{ij} \tag{22}$$

where the correction vector β is given by

$$\beta(\mathbf{x}_i) = \begin{bmatrix} \beta_0 \\ \beta_{1x} \\ \beta_{1z} \end{bmatrix} = \mathbf{A}^{-1} \begin{bmatrix} 1 \\ 0 \\ 0 \end{bmatrix} \tag{23.1}$$

$$\mathbf{A} = \sum_j W_{ij} \tilde{\mathbf{A}} \frac{m_j}{\rho_j} \tag{23.2}$$

$$\tilde{\mathbf{A}} = \begin{bmatrix} 1 & (x_i - x_j) & (z_i - z_j) \\ (x_i - x_j) & (x_i - x_j)^2 & (z_i - z_j)(x_i - x_j) \\ (z_i - z_j) & (x_i - x_j)(z_i - z_j) & (z_i - z_j)^2 \end{bmatrix} \tag{23.3}$$

Similar to the Shepard filter the density correction should be applied every m time steps.

2.6.2 *Kernel and kernel gradient corrections*

Some kernel corrective terms for improving the accuracy of kernel and kernel gradient estimations on a set of interpolation points are available in the literature (Belytschko *et al.* 1998, Bonet and Lok 1999, Vila 1999, Chen and Beraun 2000). Here we will describe some of them. Strictly speaking, operations that correct the kernel gradient no longer preserve the momentum conserving properties of the SPH method (Vaughan *et al.* 2008); however, the potential gain in accuracy and stability means that these techniques still possess unique attractions (Oger *et al.* 2007).

2.6.2.1 Kernel correction

The method was proposed by Bonet and Lok (1999) and, in an alternative form, by Liu *et al.* (1997). The kernel is modified to ensure that polynomial functions are exactly interpolated up

to a given degree. In spite of the first-order correction (linear correction) is described in detail in Bonet and Lok (1999), the same authors consider that the linear correction is unsuitable for computational purposes. They also propose using constant, rather than linear, correction. So, a vectorial variable ($\mathbf{f}_i$) can be expressed as

$$\mathbf{f}_i = \frac{\sum_j \frac{m_j}{\rho_j}\mathbf{f}_j W_{ij}}{\sum_j \frac{m_j}{\rho_j} W_{ij}} \tag{24}$$

2.6.2.2 Kernel gradient correction

The corrected kernel gradient $\tilde{\nabla} W_{ij}$ should be used to calculate the forces in the equation of motion instead of the normal kernel gradient ∇W_{ij}, being

$$\tilde{\nabla} W_{ij} = \mathbf{L}_i \nabla W_{ij} \tag{25.1}$$

$$\mathbf{L}_i = \mathbf{M}_i^{-1} \tag{25.2}$$

$$\mathbf{M}_i = \sum_j^{\text{num}} \frac{m_j}{\rho_j} \nabla W_{ij} \otimes (\mathbf{x}_i - \mathbf{x}_j) \tag{25.3}$$

where num is the number of particles interacting with particle i.

Considering, for the sake of clarity, a 2D medium, the diagonal elements of M_i are defined positive since

$$\nabla W_{ij} = \frac{dW}{dr}\frac{1}{r_{ij}}(\mathbf{x}_i - \mathbf{x}_j) \tag{26}$$

with $r_{ij} = \|\mathbf{x}_i - \mathbf{x}_j\|$ resulting in

$$M_i(1,1) = \left(-\sum_{j=1}^{\text{num}} \frac{m_j}{\rho_j}\frac{dW}{dr}\frac{1}{r_{ij}}(x_i - x_j)^2 \right) \tag{27}$$

with $dW/dr < 0$.

The same can be proved for

$$M_i(2,2) = \left(-\sum_{j=1}^{\text{num}} \frac{m_j}{\rho_j}\frac{dW}{dr}\frac{1}{r_{ij}}(z_i - z_j)^2 \right) \tag{28}$$

On the other hand, $\mathbf{M}_i$ is symmetric since

$$M_i(1,2) = M_i(2,1) = -\left(\sum_{j=1}^{\text{num}} \frac{m_j}{\rho_j}\frac{dW}{dr}\frac{1}{r_{ij}}(x_i - x_j)(z_i - z_j) \right) \tag{29}$$

Note that matrix $\mathbf{M}$ and its inverse $\mathbf{L}$ are equal to the identity matrix when the particle i is placed far from the boundaries or the free- surface. In this case, there is no real correction on the kernel gradient (on the force). Nevertheless, when the particle i is placed near the boundaries or the free-surface, the distribution of particles around it is not symmetric anymore. Thus, both $\mathbf{M}$ and $\mathbf{L}$ are different from the identity matrix and the kernel gradient is corrected following

$$\begin{bmatrix} \tilde{\nabla} W_x \\ \tilde{\nabla} W_z \end{bmatrix} = \begin{bmatrix} L_i(1,1) & L_i(1,2) \\ L_i(2,1) & L_i(2,2) \end{bmatrix} \begin{bmatrix} \nabla W_x \\ \nabla W_z \end{bmatrix} \tag{30}$$

where the subscripts x and z represent the spatial coordinates. Note that the correction is anisotropic since the terms $L_i(1,2)$ and $L_i(2,1)$ involve both spatial coordinates.

2.6.2.3 Kernel and kernel gradient correction

A simple corrective kernel and kernel derivative correction technique was developed by Chen *et al.* (1999) combining a standard SPH approach and a Taylor series expansion. In 1-D, using a Taylor series expansion in the neighborhood of x, the corrected kernel approximation for a variable f_i (e.g. the velocity) is

$$f_i = \frac{\sum_j \frac{m_j}{\rho_j} f_j W_{ij}}{\sum_j \frac{m_j}{\rho_j} W_{ij}} \tag{31}$$

and the corrective estimate of first-order derivatives becomes

$$A_i \nabla f_i = F_i \tag{32}$$

where

$$A_i = \sum_j \frac{m_j}{\rho_j}\left(x_j - x_i\right)\nabla_i W_{ij} \tag{33}$$

and

$$F_i = \sum_j \frac{m_j}{\rho_j}\left(f_j - f_i\right)\nabla_i W_{ij} \tag{34}$$

The method, which can be used for vectors and scalars, can be generalized to higher space dimensions (Chen and Beraun 2000). Thus, for example, in 2-D, the correction is obtained by solving the equation

$$A_{\mu\nu i} f_{\nu i} = F_{\mu i} \tag{35}$$

where

$$A_{\mu\nu i} = \sum_j \frac{m_j}{\rho_j}\left(\nu_j - \nu_i\right) W_{ij,\mu} \tag{36}$$

and

$$F_{\mu i} = \sum_j \frac{m_j}{\rho_j}\left(f_j - f_i\right) W_{ij,\mu} \tag{37}$$

in which μ and ν represent the spatial coordinates x and z, and $W_{ij,\mu} = \partial W_{ij}/\partial \mu_j$.

3 Governing equations

3.1 *Introduction*

In general, the fluid is considered slightly compressible in SPH, although some authors have developed an incompressible version of the method as mentioned above (Shao and Lo 2003, Gotoh *et al.* 2004, Shao 2005, Lee *et al.* 2008). Here we will describe the slightly compressible version of SPH, which is the most commonly used approach for modeling water flows in SPH.

3.2 *Conservation of mass*

The conservation law for a compressible fluid can be written in Eulerian form as

$$\frac{\partial \rho}{\partial t} + \text{div}(\rho \mathbf{u}) = 0 \tag{38}$$

In Lagrangian form, the mass of fluid associated to node i is constant as mentioned above. Thus, the previous expression can

be re-written in Lagrangian form as

$$\frac{1}{\rho}\frac{d\rho}{dt} = -\text{div}(\mathbf{u}) \tag{39}$$

which can be integrated over the domain v after multiplying both sides of the equation by the kernel

$$\int_v \frac{1}{\rho}\frac{d\rho}{dt} W(\mathbf{s}-\mathbf{x}, h)dv = -\int_v \text{div}(\mathbf{u}) W(\mathbf{s}-\mathbf{x}, h)dv \tag{40}$$

By the reproducing nature of the kernel, Eq. (1), the left side is $(1/\rho)(d\rho/dt)$ evaluated at position $\mathbf{s}$ and the right side can be rewritten as

$$-\int_v [\text{div}(W(\mathbf{s}-\mathbf{x}, h)\mathbf{u}) - \mathbf{u}\nabla W(\mathbf{s}-\mathbf{x}, h)]dv \tag{41}$$

Using the Gauss's theorem

$$\frac{1}{\rho}\frac{d\rho}{dt} = \int_v \mathbf{u}\nabla W(\mathbf{s}-\mathbf{x}, h)dv - \int_S W(\mathbf{s}-\mathbf{x}, h)\mathbf{u}\mathbf{n}\, dS \tag{42}$$

where the last integral is a surface integral over the surface S that encloses the volume v and $\mathbf{n}$ is a unit vector normal to the surface and pointing outward. This integral can be neglected when the surface is far from point $\mathbf{s}$ since the kernel function goes to zero rapidly. In simulations, this condition is often not met as pointed out by Belytschko *et al.* (1998), which can lead to problems in accuracy.

In continuous form the equation becomes

$$\frac{1}{\rho}\frac{d\rho}{dt} = \int_v \mathbf{u}\nabla W(\mathbf{s}-\mathbf{x}, h)dv \tag{43}$$

which can be rewritten in discrete form as

$$\left(\frac{1}{\rho}\frac{d\rho}{dt}\right)_i = \sum_j \frac{m_j}{\rho_j}\mathbf{u}_j \nabla W_{ij} \tag{44}$$

Due to the symmetry of the gradient, its first derivative fulfills $\nabla_i W_{ij} = -\nabla_j W_{ij}$ which results in

$$\left(\frac{1}{\rho}\frac{d\rho}{dt}\right)_i = -\sum_j \frac{m_j}{\rho_j}\mathbf{u}_j \nabla_i W_{ij} \tag{45}$$

Once again, Monaghan's second golden rule should be invoked to obtain an equation where the evolution of the variable under scope depends on the difference between particles i and j. From Eq. (14) the gradient of a constant is zero, so

$$0 = \sum_j \frac{m_j}{\rho_j}\nabla_i W_{ij} \tag{46}$$

Multiplying by $\mathbf{u}_i$, this zero term can be added to Eq. (45) to obtain

$$\left(\frac{d\rho}{dt}\right)_i = \rho_i \sum_j \frac{m_j}{\rho_j}(\mathbf{u}_i - \mathbf{u}_j)\cdot\nabla_i W_{ij} \tag{47}$$

A different interpolant

$$\rho_i = \sum_j m_j \nabla_i W_{ij} \tag{48}$$

which permits calculating the density as the summation over the neighboring particles instead of solving a new differential equation. Nevertheless, this last equation is not the best option in fluid calculations since it leads to a density drop near the free surface of the fluid as stated by Monaghan (1992). On the other, using Eq. (47) the density varies when the particles move relative to each other.

3.3 *Conservation of momentum*

The equation that governs the fluid motion can be derived in particle form using the same method as considered for the conservation of mass. If we consider the system in the absence of viscosity (a special treatment for viscosity will be considered later), the equation of motion in its Lagrangian form becomes

$$\frac{d\mathbf{u}}{dt} = -\frac{1}{\rho}\nabla p - \mathbf{g} \tag{49}$$

The following change of variable can be considered to symmetrize the pressure gradient

$$\frac{\nabla p}{\rho} = \nabla\left(\frac{p}{\rho}\right) + \frac{p}{\rho^2}\nabla\rho \tag{50}$$

In such a way that the equation of momentum for particle i becomes

$$\left(\frac{d\mathbf{u}}{dt}\right)_i = -\sum_j m_j \left(\frac{p_j}{\rho_j^2} + \frac{p_i}{\rho_i^2}\right)\nabla_i W_{ij} - \mathbf{g} \tag{51}$$

This expression is, possibly, the most commonly used to describe the gradient of pressure in SPH although other authors (Bonet and Look 1999) consider that the expression

$$-\sum_j \frac{1}{\rho_i \rho_j} m_j (p_j + p_i)\nabla_i W_{ij} \tag{52}$$

for the pressure gradient is variationally consistent with the use of Eq. (39).

3.4 *Viscosity*

The viscosity plays a key role in preventing instabilities in fluid motion, where single particles can move in a rather chaotic way. These instabilities can be prevented by means of viscous terms, which should be added to the previous momentum equation. Different viscosity treatments have been considered in the literature, an overview on numerical modeling of complex turbulent free-surface flows within the SPH context can be seen in Violeau and Issa (2007). Here we will only refer to the most commonly used methods to describe viscosity free-surface flows.

3.4.1 *Artificial viscosity*

The artificial viscosity proposed by Monaghan (1992) has been used very often due to its simplicity. In SPH notation, the momentum equation can be written as

$$\frac{d\mathbf{u}_i}{dt} = -\sum_j m_j \left(\frac{p_j}{\rho_j^2} + \frac{p_i}{\rho_i^2} + \Pi_{ij}\right)\nabla_i W_{ij} - \mathbf{g} \tag{53}$$

where Π_{ij} is the viscosity term:

$$\Pi_{ij} = \begin{cases} \dfrac{-\alpha\overline{c_{ij}}\mu_{ij}}{\overline{\rho_{ij}}} & \mathbf{u}_{ij}\,\mathbf{x}_{ij} < 0 \\ 0 & \mathbf{u}_{ij}\,\mathbf{x}_{ij} > 0 \end{cases} \tag{54}$$

with $\mu_{ij} = (h\mathbf{u}_{ij}\,\mathbf{x}_{ij})/(r_{ij}^2 + \eta^2)$; where, $\mathbf{u}_{ij} = \mathbf{u}_i - \mathbf{u}_j$ and $\mathbf{x}_{ij} = \mathbf{x}_i - \mathbf{x}_j$, $\overline{c_{ij}} = (c_j + c_i)/2$ being the mean speed of sound. The parameter $\eta^2 = 0.01\,\mathrm{h}^2$ is included to avoid singularities and α is a free parameter that can be changed according to each problem, thus making the approach empirical. There was an additional term depending on μ_{ij}^2 in the original formulation (Monaghan 1992) which is not usually considered in fluid problems (Monaghan 1994).

3.4.2 *Laminar viscosity*

An additional formulation for viscosity was proposed by Morris *et al.* (1997) to solve problems involving low Reynolds number flows. The momentum equation can then be re-written as

$$\frac{du_i}{dt} = -\sum_j m_j \left(\frac{p_j}{\rho_j^2} + \frac{p_i}{\rho_i^2}\right)\nabla_i W_{ij} - \mathbf{g} + \sum_j m_j \left(\frac{4\upsilon_0 \mathbf{x}_{ij}\nabla_i W_{ij}}{(\rho_i + \rho_j)(r_{ij}^2 + \eta^2)}\right)\mathbf{u}_{ij} \tag{55}$$

where, in general, the kinetic viscosity of laminar flow υ_0 is on the order of $10^{-6}\,\mathrm{m^2 s^{-1}}$ for water.

3.4.3 *Laminar viscosity and Sub-Particle Scale (SPS) turbulence*

The artificial viscosity represents viscosity in a phenomenological way and prevents particles from interpenetration. In addition, it helps to keep numerical stability of the computational scheme. Nevertheless, the method is too dispersive affecting shear and, even, fluid propagation, especially when the flow is not dominated by its gravitational component. On the other hand, the laminar viscosity proposed by Morris *et al.* (1997) is accurate for low Reynolds number flows but does not capture the main features of the flow when turbulent terms are involved.

Using the concepts of Large Eddy Simulation (LES), the Sub-Particle Scale (SPS) approach to modeling turbulence was first described by Gotoh *et al.* (2001) to represent the effects of turbulence in their MPS model and adapted to SPH by Shao and Gotoh (2005) and Dalrymple and Rogers (2006). SPS scaling for a compressible fluid requires a spatial averaging methodology as Favre-averaging. The momentum conservation equation can be written as

$$\frac{d\mathbf{u}}{dt} = -\frac{1}{\rho}\nabla p - \mathbf{g} + \upsilon_0\nabla^2\mathbf{u} + \frac{1}{\rho}\nabla\tilde{\tau} \tag{56}$$

where the three first terms on the right hand side (pressure gradient, gravitation and laminar terms) can be treated following Eq. (55) and $\tilde{\tau}$ represents the SPS stress tensor given by

$$\tilde{\tau}_{\mu\nu} = \bar{\rho}\left(2\upsilon_t\tilde{S}_{\mu\mu} - \frac{2}{3}\tilde{S}_{\kappa\kappa}\delta_{\mu\nu} - \frac{2}{3}C_I\Delta l^2\delta_{\mu\nu}\right) \tag{57}$$

where $C_I = 0.0066$, following (Dalrymple and Rogers 2006); Δl is the particle-particle spacing and the Favre-filtered rate of strain tensor is

$$\tilde{S}_{\mu\nu} = -\frac{1}{2}\left(\frac{\partial u_\mu}{\partial x_\nu} + \frac{\partial u_\nu}{\partial x_\mu}\right) \tag{58}$$

A standard Smagorinsky model (Smagorinsky 1963) is used to determine the eddy viscosity

$$\upsilon_t = [\min(C_s\Delta l)]^2|\tilde{S}| \tag{59}$$

being $C_s = 0.12$ the Smagorinsky constant and the local strain rate $|\tilde{S}| = (2S_{\mu\nu}S_{\mu\nu})^{1/2}$. Thus, the SPS stress can be discretized in symmetric form as

$$\frac{1}{\rho_i}\left(\frac{\partial\tilde{\tau}_{\mu\nu}}{\partial x_\nu}\right)_i = \sum_j m_j\left(\frac{(\tilde{\tau}_{\mu\nu})_j}{\rho_j^2} + \frac{(\tilde{\tau}_{\mu\nu})_i}{\rho_i^2}\right)\frac{\partial W_{ij}}{\partial x_\nu} \tag{60}$$

3.5 *Equation of state*

Following (Batchelor 1974, Monaghan 1994), the relationship between pressure and density is assumed to follow the expression:

$$p = B\left[\left(\frac{\rho}{\rho_0}\right)^\gamma - 1\right] \tag{61}$$

where γ is a constant between 1 and 7 (although 7 is used in most of the oceanic applications) $\rho_0 = 1000\,\mathrm{kg\,m^{-3}}$ being the reference density, usually at the free surface. The main advantage of this approach is that there is no need to solve an additional partial differential equation for pressure (Poisson equation) that can become time consuming. In addition, solving the Poisson equation involves determining the free surface, which is not straightforward in most of the cases, especially in those with wave breakings and loss of continuity in the fluid. Unfortunately, these are precisely the cases where the SPH can show a higher performance compared to grid based methods. Nevertheless, several authors (Lee *et al.* 2008, Lee *et al.* 2009) have considered this incompressible approach with accurate results.

The speed of sound depends on the derivative of pressure with respect to density

$$c^2(\rho) = \frac{\partial p}{\partial\rho} = \frac{B\gamma}{\rho_0}\left(\frac{\rho}{\rho_0}\right)^{\gamma-1} \tag{62}$$

In such a way that, $B = c_0^2\rho_0/\gamma$, c_0 being the speed of sound at the reference density. Realistic speeds of sound cannot be used for computational purposes since the associated time step imposed by the Courant-Friedrich-Levy is too small. Following Monaghan and Kos (1999), the speed of sound can be artificially slowed with accurate results in fluid propagation (not in sound propagation). Nevertheless, the speed of sound should be, at least, 10 times higher than the maximum fluid velocity expected in the flow (Monaghan and Kos 1999). Monaghan (1994) also indicates for wave problems that the sound speed in models should be at least 10 times the water wave speed. Further they show that the value of γ is not very important once that criterion is met. In spite of the fluid being treated as weakly compressible, other authors have preferred alternative incompressible formulations as we mentioned above.

3.6 *Moving the particles*

Particles are moved using the XSPH variant due to Monaghan (Monaghan 1989).

$$\frac{d\mathbf{x}_i}{dt} = u_i + \varepsilon \sum_j \frac{m_j}{\overline{\rho_{ij}}} \mathbf{u_{ij}} W_{ij} \tag{63}$$

where $0 \leq \varepsilon \leq 1$ is a constant and $\overline{\rho_{ij}} = (\rho_i + \rho_j)/2$. This method moves the particle with a velocity that is close to the average velocity in its neighborhood.

3.7 *Tensile instability*

Most of the kernels described in section 2.3 have a maximum in their first derivative in such a way that the forces between particles go to zero in the equation of motion with decreasing inter-particle spacing. Note that both the body and shear forces in the momentum equation depend on the first derivative of the kernel. This so-called tensile instability manifests itself as particles clumping together unrealistically. In the case of fluids, a tensile correction proposed by Monaghan (2000) removes the instability by adding an artificial pressure.

$$\frac{p_k}{\rho_k^2} \rightarrow \frac{p_k}{\rho_k^2}(1 + R_k \Psi^n) \tag{64}$$

where the subscript k represents the particle (i or j), n is an integer (usually 4), $\Psi = W(q)/W(q_{\min})$ is the ratio between the kernel at q (the present interparticle spacing) and at $q_{\min}$, the distance at which the first derivative of the kernel reaches the local minimum; and R_k is a coefficient.

$$R_k = \begin{cases} 0.006 & \text{if } p_k > 0 \\ 0.6 & \text{if } p_k < 0 \end{cases} \tag{65}$$

4 Implementation

4.1 *Boundary conditions*

The boundary conditions do not appear in a natural way in the SPH formalism. When a fluid particle approaches a solid boundary, only the particles located inside the domain are included in the SPH interpolants, without any interaction from the outside. The incompleteness of the kernel can generate unrealistic effects, due to the different nature of the variables to solve, since some, such as the velocity, fall to zero when they approach the boundaries, while others, such as the density, do not. The different solutions to avoid boundary problems consist of the creation of several virtual particles that characterize the limits of the domain. Basically, three different types of boundaries can be distinguished:

Ghost particles. Randles and Libersky (1996) considered boundary particles whose properties, included their position, vary each time step. When a real particle is close to a contour (at a distance shorter than the kernel smoothing length) then a virtual (ghost) particle is generated outside of the system, constituting the mirror image of the incident one with respect to the boundary. Both particles have the same density and pressure, but opposite velocity, so creating a repulsion mechanism. One of the main drawbacks is that the number of boundary particles varies each time step, which complicates its implementation in the code. In addition, the real position of the boundary with respect to which the ghost particle will be created is difficult to be univocally determined in complex geometries. Indeed, modeling complex geometries with ghost particles, in particular sharp edges and arbitrarily curved surfaces in 3-D, represents the biggest drawback of this technique. Similar to the idea of ghost particles, Hieber and Koumoutsakos (2008) use regularized SPH (rSPH) to incorporate the Immersed Bounday Method (IBM), however, at present this approach requires the non-existence of a free-surface.

Repulsive particles. This type of boundary technique is due to Monaghan (1994). In this case the particles that constitute the frontier exert central forces on the fluid particles, in analogy with the forces among molecules. Thus, for a boundary particle and a fluid particle separated a distance r, the force for unit of mass has the form given by the Lennard-Jones potential. In a similar way, other authors (Peskin 1977) express this force assuming the existence of forces in the boundaries, which can be described by a delta function. This method was refined in Monaghan and Kos (1999) by means of an interpolation process, minimizing the inter-spacing effect of the boundary particles on the repulsion force of the wall. Finally, the method proposed by Monaghan and Kos (1999) can be modified to adjust the magnitude of the force according to the local water depth and velocity of the water particle normal to the boundary. This method is described in detail in Rogers and Dalrymple (2008). The calculation of normals and tangents to the surface is not easy in complex geometries. In addition, the dependence of the force on water depth and velocity can be a source of numerical instabilities. Similar to this approach there is also the work of Kulasegaram *et al.* (2004) who use the variational approach as the initial start for a new boundary condition which eventually uses an empirical function to account for the lack of complete kernel support.

Dynamic particles. These particles verify the same equations of continuity and of state as the fluid particles, but their position remains unchanged or is externally imposed. An interesting advantage of these particles is their computational simplicity, since they can be calculated inside the same loops as fluid particles. In this method, boundary particles are forced to satisfy the same equations as fluid particles. Thus, they follow the continuity equation and the equation of state described in previous section and they are included in the momentum equation of the fluid particles. However, they do not move according to a momentum equation but they remain fixed in position (fixed boundaries) or move according to some externally imposed function (moving objects like gates, and wavemakers), Dalrymple and Knio (2001).

These particles have been previously used to study the interaction between waves and coastal structures (Gómez-Gesteira and Dalrymple 2004, Gómez-Gesteira *et al.* 2005, Crespo *et al.* 2007b, Crespo *et al.* 2008). The method is described in detail in Crespo *et al.* (2007a) and Gómez-Gesteira *et al.* (2009).

The main problem of this boundary is the evolution from the initial condition. When the particles start moving and separate from the walls the density decreases locally, which generates

a pressure decrease that results in a "*pseudo-viscosity*" forcing small groups of particles to remain stuck on the wall. This also has the effect of generating a larger than physical boundary layer. Finally, the technique does not guarantee that the fluid particles do not penetrate through the boundary in an unphysical way — a problem that does not exist with the other techniques.

In summary, the creation of realistic boundary conditions is still an open topic in SPH methods and new research should be conducted. Several attempts to improve the accuracy of the boundary treatment have been carried out during the last few years, such as the method proposed by Marongiu *et al.* (2007) to simulate flows on Pelton turbines being one the most promising advances.

4.2 *Variable time step*

To march the simulations forward in time, all SPH schemes use time integration schemes which should be at least second-order accurate since the particles are moving in space. In the results presented herein, either a second-order predictor-corrector (Monaghan 1994) or a Verlet scheme is used (Verlet 1967). The time step is strongly dependent on the flow properties. Thus, for example, the time step decreases when the fluid collides with a fixed boundary, since the forces increase suddenly; or after the formation of a water splash, where the velocities increase. In general, the time-step control should be dependant on the CFL condition, the forcing terms and the viscous diffusion term (Monaghan 1989). A variable time step Δt is calculated according to Monaghan and Kos (1999):

$$\Delta t = C \cdot \min(\Delta t_f, \Delta t_{cv}) \tag{66.1}$$

$$\Delta t_f = \min_i(\sqrt{h/|f_i|}) \tag{66.2}$$

$$\Delta t_{cv} = \min_i \frac{h}{c_s + \max_j \left| \frac{h\mathbf{u_{ij}}\mathbf{x}_{ij}}{r_{ij}^2} \right|} \tag{66.3}$$

Here Δt_f is based on the force per unit mass $|f_i|$, and Δt_{cv} combines the Courant and the viscous time-step controls. C is a constant on the order of 0.1.

There are a variety of methods to march the solution of SPH equations in time. In general, it is advisable to use at least a second order accurate scheme in time. For a description of different schemes usually considered in SPH the reader is referred to Dalrymple *et al.* (2009) and Gomez-Gesteira *et al.* (2009).

4.3 *Computational efficiency: link list*

Following Monaghan and Lattanzio (1985) the computational domain is divided into square cells of side nh, where n depends on the particular choice of the kernel as mentioned above. Thus, for a particle located inside a cell, only the interactions with the particles of neighboring cells need to be considered. In this way the number of calculations per time step diminishes from N^2 operations to the order of N, being N the number of particles. This results in considerable saving in computational time. For a complete description of link lists the reader is referred to Viccione *et al.* (2008).

5 Results

5.1 *Introduction*

As we mentioned above, different test cases will be used to depict the main features of SPH method and its capability to reproduce experimental results accurately. In particular, the model SPHysics (Gomez-Gesteira *et al.* 2009) will be considered to run the different study cases.

5.2 2D *Dam break over dry bed*

SPHysics will be used to analyze the collapse due to the gravity of water column in a tank. A complete description of the experiment (Fig. 1) can be obtained from Koshizuka and Oka (1996). The same setup was used by Violeau and Issa (2007) and Crespo *et al.* (2007a) to check the accuracy of their SPH codes. The tank is 4 m long, the initial volume of water is 1 m long and its height 2 m. The numerical experiment will be considered 2D since the third dimension (the width) is negligible for the phenomenon under scope.

The system was solved with a predictor-corrector algorithm (Monaghan 1989), using a cubic-spline kernel (Monaghan and Latanzio 1985), dynamic boundary conditions (Crespo *et al.* 2007a), artificial viscosity, $\alpha = 0.5$, and the XSPH correction (Monaghan 1989) with $\varepsilon = 0.5$ to smooth gradients in fluid particles movement. Fluid particles were initially placed on a staggered grid with zero initial velocity. Nodes of the grid are located at $R = l\,dx\,\mathbf{i} + m\,dz\,\mathbf{k}$ with a two-point basis $(0, 0)$ and $(dx/2, dz/2)$ referred to the corner defined by R. l and m are integers, $\mathbf{i}$, $\mathbf{k}$ are unit vectors in x- and z-directions. Fixed particles (bottom and walls) were placed in two rows forming a staggered grid with the same interspacing as the fluid particles.

From now on, the standard case will correspond to $dx = dz = 0.012$ m, $h = 0.0156$ m (29,723 particles) and without density filter or kernel correction. Additional cases will be run for different discretizations (h), density filters and kernel corrections.

Figure 2 shows the velocity magnitude (standard case) at different instants of dam evolution where the color of each particle corresponds to its instantaneous velocity. The colorbar is common to all snapshots. Distances are in meters and velocities in meters per second. At $t = 0.40$ s the dam break has evolved

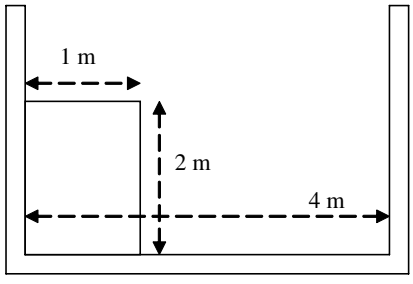

Figure 1 Initial configuration of the water column and the tank

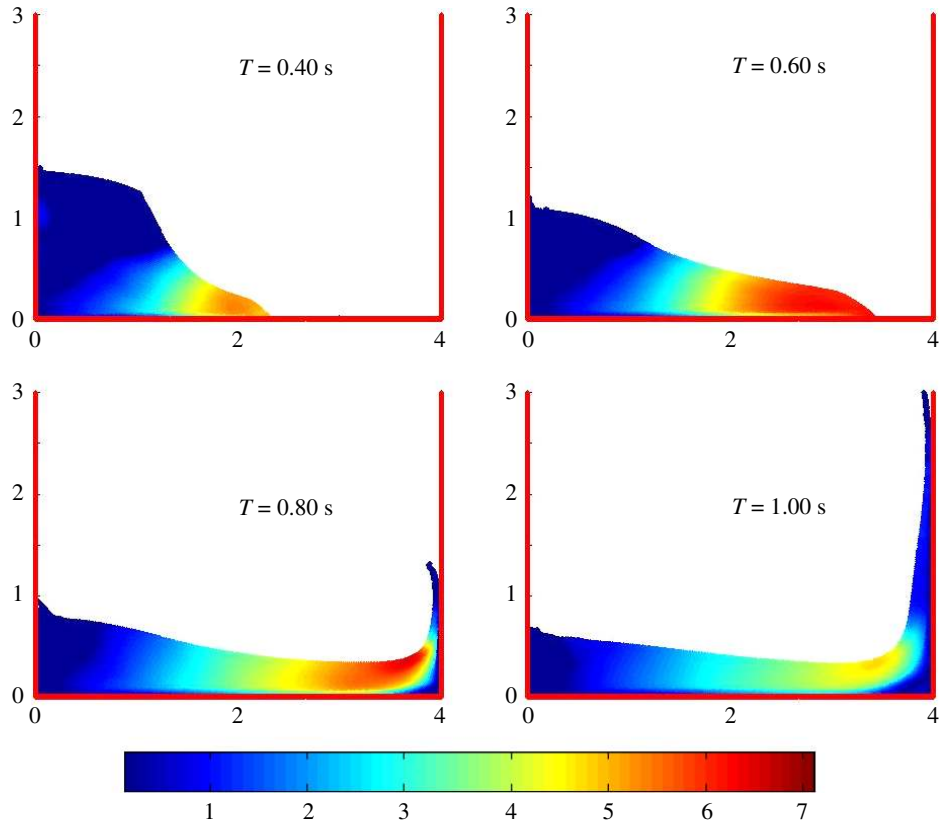

Figure 2 Collapse of a water column in a tank simulated with SPH model plotting the particle velocities

from its initial square-shaped configuration, forming a toe where the maximum velocities can be observed. The toe velocity evolution will be compared with experimental data in next figure. At $t = 0.60$ s the wave front has approached the right wall. In $t = 0.80$ s the water has collided with the right wall and generated a splash. Note that water velocity in the bulk of the fluid is much faster than at the splash zone. At $t = 1.00$ s water is observed to climb onto the right wall.

The movement of the fluid inside the box is dependent on the fluid movement near the dam toe. Figure 3 shows how SPHysics fits the experimental position of the toe (X in meters) provided by Koshizuka and Oka (1996) in an accurate way. Dots correspond to experimental values and solid lines to different realizations of the same experiment with different smoothing lengths. In particular, $h = 0.0156$ m (29723 particles), $h = 0.0260$ m (11203 particles) and $h = 0.0390$ m (5156 particles) were considered with a similar accuracy in the comparison with experimental data. Actually, the square of the correlation coefficient between experimental and numerical data, R^2, is higher than 0.99 in all cases.

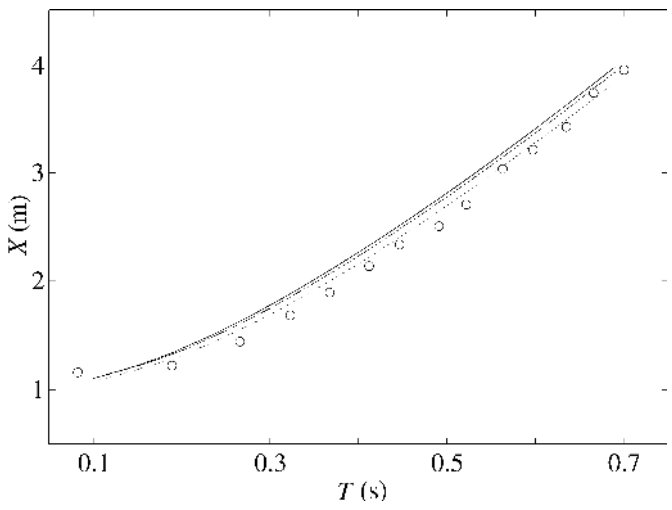

Figure 3 Dam break over a dry bed. Lines represent the X position of the dam toe for different numerical discretizations ($h = 0.0156$ m, $h = 0.0260$ m and $h = 0.0390$ m). Dots represent experimental data

The observed difference between numerical and experimental results can be quantified by means of two statistical parameters.

$$A_r = \left(\sum_i (\mathrm{Var}_i^{\mathrm{num}})^2 \Big/ \sum_j (\mathrm{Var}_i^{\mathrm{exp}})^2 \right)^{1/2} \tag{67.1}$$

$$P_d = \left(\sum_i (\mathrm{Var}_i^{\mathrm{num}} - \mathrm{Var}_i^{\mathrm{exp}})^2 \Big/ \sum_j (\mathrm{Var}_i^{\mathrm{exp}})^2 \right)^{1/2} \tag{67.2}$$

where "Var" is the variable under scope (horizontal velocity of the dam toe in this case) and the superscripts refer to experimental or numerical values. The first parameter, A_r, represents the relative amplitude of both signals, in such a way that a perfect agreement between experimental and numerical data would result in $A_r \to 1$. On the other hand, the second parameter, P_d, is the phase difference between both signals, a perfect agreement would result in $P_d \to 0$. Table 1 summarizes the values of A_r and P_d obtained for the different smoothing length values. Although both statistical parameters show a satisfactory

Table 1 Statistical parameters A_r and P_d for different smoothing lengths (h). The method without density filter was used in the three cases

	$h = 0.0156$ m	$h = 0.0260$ m	$h = 0.0390$ m
P_d	0.09	0.10	0.11
A_r	0.94	0.93	0.91

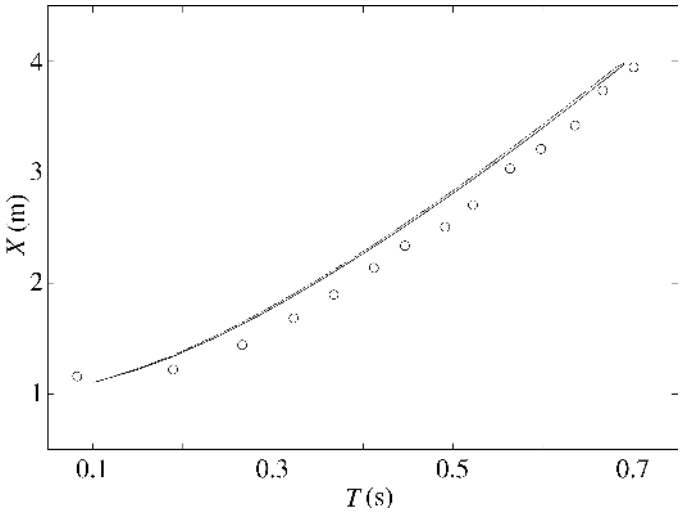

Figure 4 Dam break over a dry bed. Lines represent the X position of the dam toe for different numerical approaches (without density filter, with a Shepard density filter and with a MLS density filter). Dots represent experimental data

agreement between numerical and experimental solutions, results show to be more accurate when decreasing the smoothing length. One of the important features of SPH method is that it provides reliable results, at least referred to the toe position, even using a coarse discretization. Note that the execution time relative to the coarsest discretization is 2.5 times longer for $h = 0.0260$ m and 5 times longer for $h = 0.0156$ m.

As we mentioned above, the pressure field of the particles can exhibit large pressure oscillations, which can be smoothed out by performing a filter over the density. First of all, the toe position was calculated again for the finest discretization ($h = 0.0156$ m) without density filter (standard case), with a Shepard filter and with a MLS filter. Filters were only used every $m = 40$ time steps. Figure 4 shows how the three water front locations are practically equal. Actually, the difference between Shepard and MLS signals is on the order of the numerical roundoff. The three signals are in good agreement with the experimental data; this close agreement is because the flow is primarily a gravity-driven flow and the pressure field during this time in the simulation is still close to hydrostatic. Nevertheless, the important differences among the density fields can be observed by comparing Figs. 5 (without density filter), 6 (with a Shepard filter) and 7 (with a MLS filter). Each figure reproduces three different instants of dambreak propagation. In the first frame, $t = 0.70$ s, the toe is colliding with the front wall of the box, giving rise to local increase of density. Note that the density increase immediately results in pressure increase following Eq. (61). The formation of

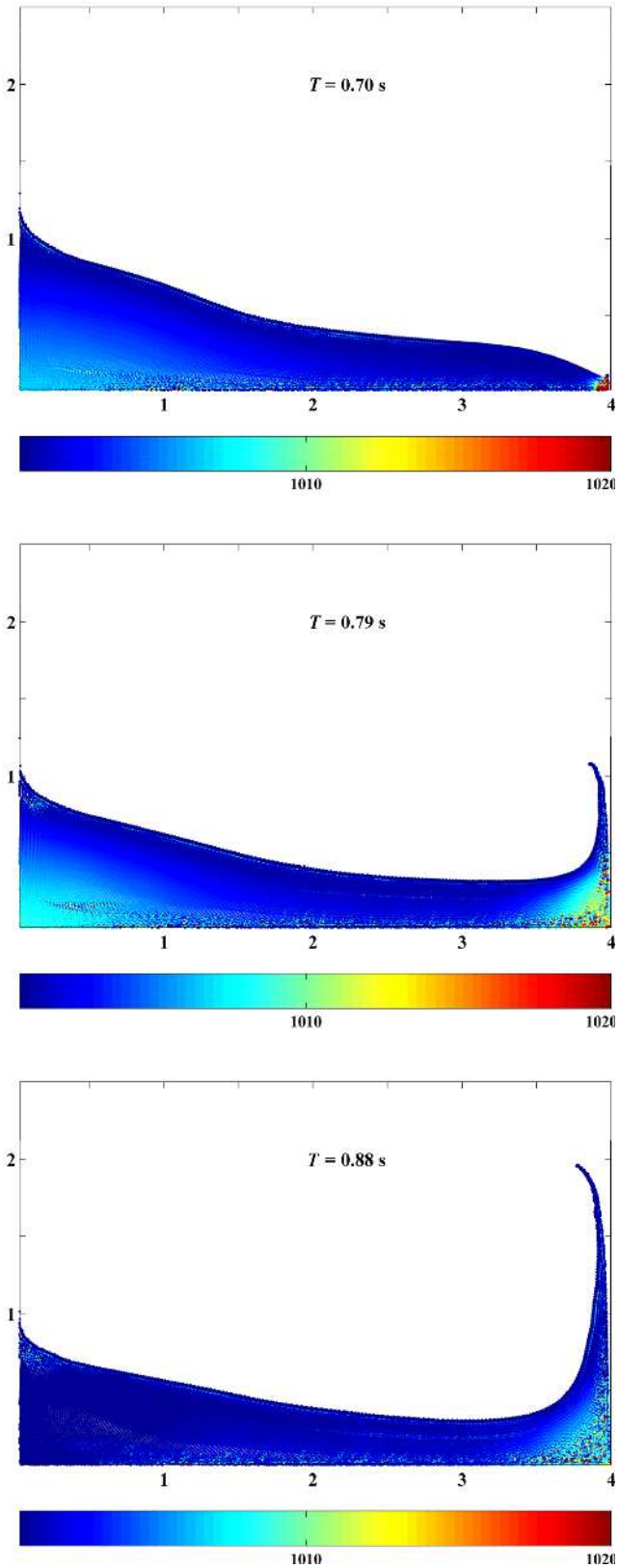

Figure 5 Dam break evolution and collision with the front wall. Calculations were run without density filter. The color of each particle corresponds to its instantaneous density in kg m^{-3}

a jet is observed in the second, $t = 0.79$ s, and third, $t = 0.88$ s, frames.

Important density oscillations can be observed in the unfiltered solution (Fig. 5). These oscillations are especially important near

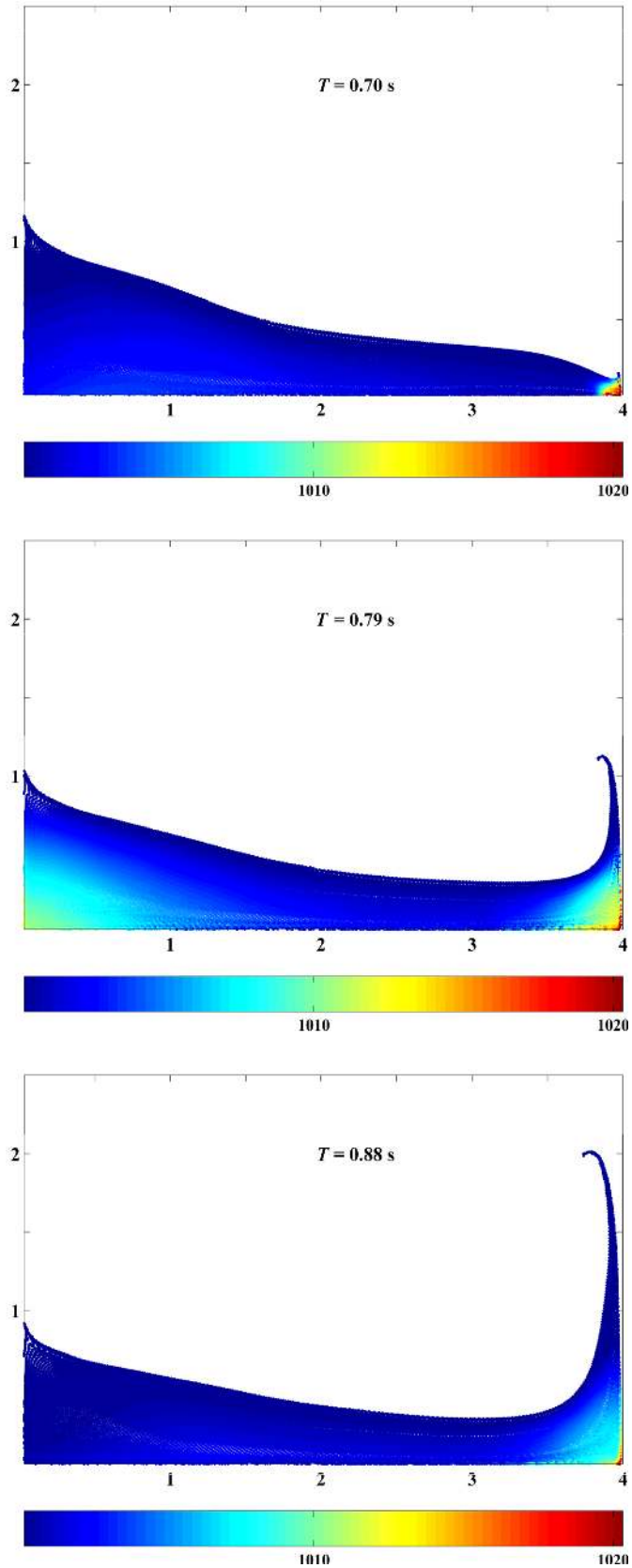

Figure 6 Dam break evolution and collision with the front wall. Calculations were run with a Shepard density filter. The color of each particle corresponds to its instantaneous density in kg m^{-3}

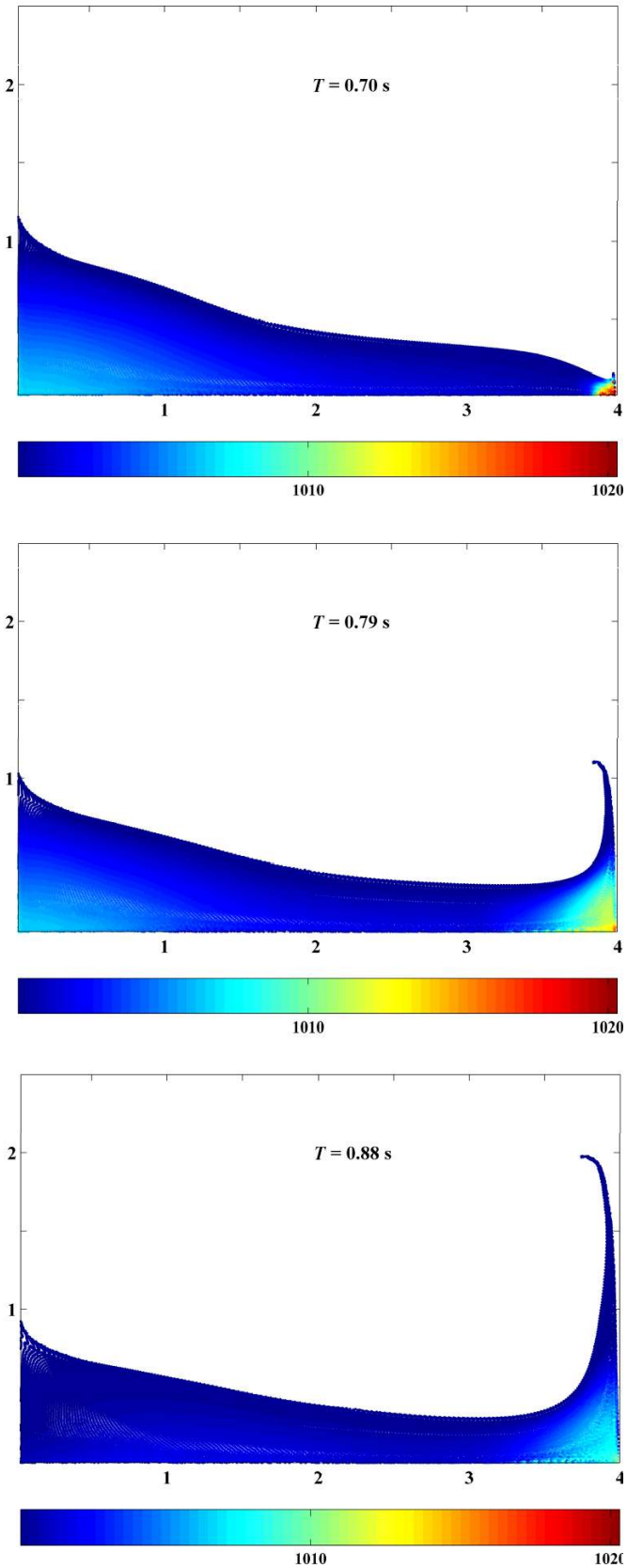

Figure 7 Dam break evolution and collision with the front wall. Calculations were run with a MLS density filter. The color of each particle corresponds to its instantaneous density in kg m^{-3}

Table 2 Statistical parameters A_r and P_d for the method without density filter and the filtered solutions (Shepard and MLS). The last column corresponds to the case without density filter but with a corrected kernel gradient (CKG). The same smoothing length ($h = 0.0156$ m) was used in all calculations

	no filter	Shepard	MLS	CKG
P_d	0.09	0.08	0.08	0.08
A_r	0.94	0.95	0.95	0.95

the lower right corner, which correspond to the region where water collides with the container, given rise to the highest pressure values. These fluctuations tend to destroy the quality of the calculated fields, especially when considering low viscosity values, Note that a rather high artificial viscosity ($\alpha = 0.5$) was used in the case under scope, which helped to stabilize the solution. The use of more realistic viscosity values would lead to unphysical density and pressure fields. The density fields obtained using Shepard (Fig. 6) and MLS (Fig. 7) filters are similar and less noisy than the ones obtained without filters (Fig. 5). Table 2 summarizes the values of A_r and P_d obtained for the different methods considering the same smoothing length ($h = 0.0156$ m). Although both statistical parameters show a satisfactory agreement between numerical and experimental solutions, the filtered methods show to be more accurate than the unfiltered one.

Apparently, the main features of the three solutions (the free-surface profile) remain practically unchanged, only small differences in shape can be observed near the jet tip in the second and third frames. Nevertheless, these initially small differences can evolve in time giving rise to unphysical results as depicted in Fig. 8, where the upper row corresponds to the unfiltered method, the middle one to the Shepard filter and the lower one to the MLS filter. Apart from the previously mentioned fluctuations in density field, the shape of the jet created after the overturning depends on the method. Thus, at $t = 1.80$ s the jet height is smaller in the unfiltered solution. At $t = 2.40$ s the jet in the unfiltered solution has suffered unphysical fragmentation and is different both in shape and position to the ones observed in the cases with density filters. In addition, the wave profile generated after overturning is also different. Bubble capture generated by two consecutive breakings of the reflected wave is reproduced by Shepard and MLS method but not by the unfiltered method. A small number of particles remain attached to the front wall ($t = 2.40$ s) in all methods due to the particular choice of boundary particles (Crespo *et al.* 2007a).

The importance of local density fluctuations can be quantified following

$$\Delta\rho = \frac{1}{M_d}\sum_{i=1}^{M}\left(\frac{\sum_{\substack{j=1\\ j\neq i}}^{M_d}|\rho_i-\rho_j|\,W_{ij}}{\sum_{\substack{j=1\\ j\neq i}}^{M_d}W_{ij}}\right) \tag{68}$$

where M_d refers to all particles inside a particular area. In particular, the area close to the lower right corner was considered, $3.5\,\text{m} \leq x_i \leq 4.0\,\text{m}$ and $0.0\,\text{m} \leq z_i \leq 0.5\,\text{m}$. Note that all interactions at a distance higher than $2h$ immediately cancel out since the kernel W_{ij} is zero. Figure 9 shows the mean density fluctuations for the three methods before and after the collision with the right wall of the container (~ 0.7 s). The fluctuations are in average 5 times higher in the case without density filter (solid line) than in the cases with Shepard (dashed line) or MLS (dotted line) filters.

In addition to the good accuracy to reproduce experimental results, the method can be observed to conserve the total energy which is the sum of kinetic, potential and thermal energy. The thermal energy associated to each particle can be calculated every time step using the expression given by (Monaghan 1992)

$$\frac{de_i}{dt} = \frac{1}{2}\sum_j m_j\left(\frac{p_j}{\rho_j^2}+\frac{p_j}{\rho_i^2}+\Pi_{ij}\right)\mathbf{u}_{ij}\nabla_i W_{ij} \tag{69}$$

Note that artificial viscosity (Eq. (54)) was considered in this particular case.

The percentage of energy increment, $\Delta E = 100(E(t)-E(t=0))/E(t=0)$, is represented in Fig. 10 for the three cases described above. The energy increase is similar in the three cases, although slightly higher (solid line) in the case without density filter and lower in case with Shepard filter. The highest energy variation is close to 0.01% in 18000 time steps lying inside the limits proposed by (Monaghan 1992). The sudden change in gradient in this curve is due to the fluid impact on the right-hand wall.

Finally, the particular choice of m (the number of time steps between two consecutive density filters) does not play a key role in this particular case and similar results can be obtained for m values ranging from 10 to 100 time steps. In general, it is advisable to use m values on that order of magnitude since higher values do not smooth out the solution and lower values have an important computational cost as previously described by Colagrossi and Landrini (2003). Apart from accuracy, an important issue is the computational cost of the density filters. The speed of the different methods was compared for a run of 3 s in real time with the smallest smoothing length ($h = 0.0156$ m) and $m = 40$. The method without density filter showed to be about 8% faster than the rest.

Figure 11 shows the X position of the dam toe for different numerical approaches. The toe position was calculated again for the finest discretization ($h = 0.0156$ m) without kernel correction (solid line) and with a kernel gradient correction (dashed line). This correction is expected to improve the fluid description near the leading edge of the dambreak, due to the deficiency in the number of particles in that zone. This improvement can be seen in the last column of Table 2, where the kernel gradient correction provides an accuracy equal to the one obtained by using density filters.

5.3 *2D Dam break over a wet bed*

SPH is an especially well suited method when the complexity of the phenomenon under investigation increases. Dam break

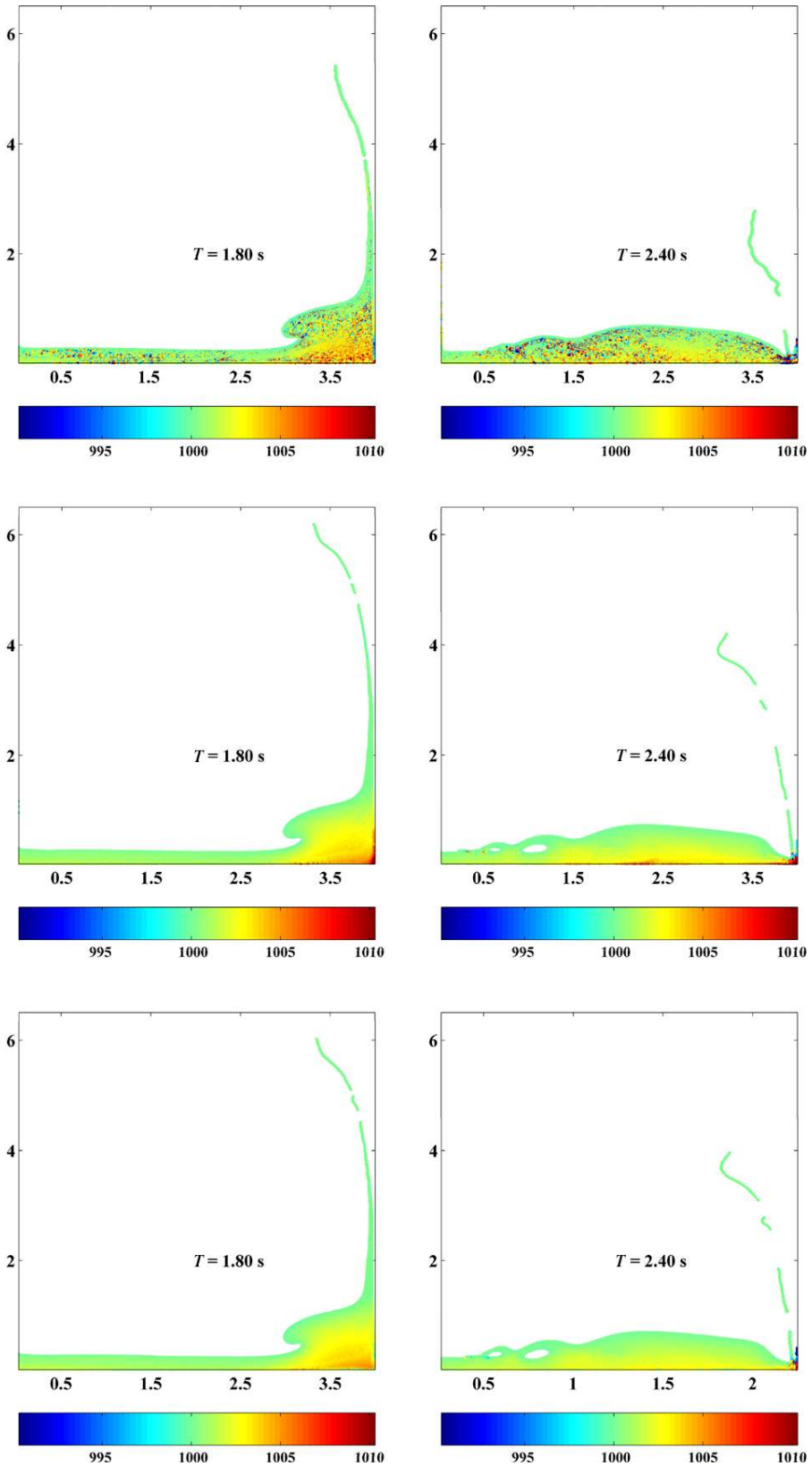

Figure 8 Dam break evolution and water overturning. Comparison among the results obtained by means of the three methods: without density filter (upper row); with Shepard filter (middle row); with MLS filter (lower row). Both the density distribution and the jet and wave profile are observed to be different in the case without filter

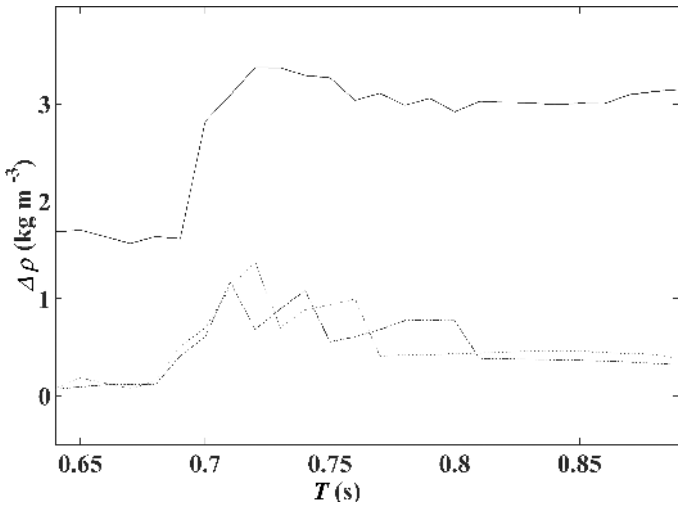

Figure 9 Mean density fluctuation (in kg m^{-3}) for the three methods before and after the collision with the front wall in the vicinity of the right lower corner of the container. Density fluctuations are much higher in the calculation without density filter (solid line)

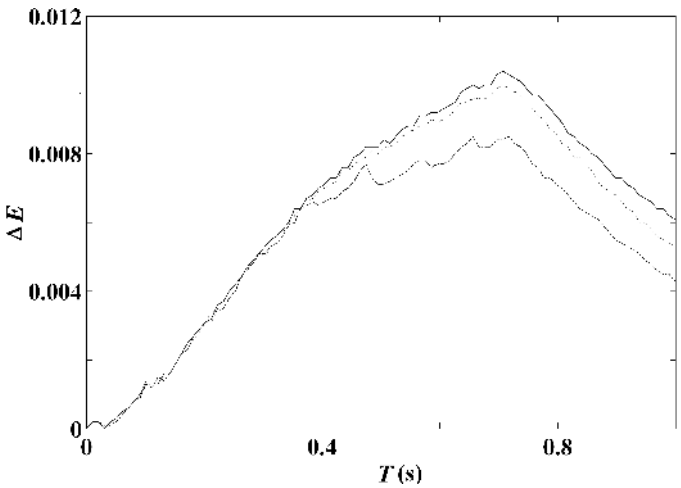

Figure 10 Energy change (in percentage) for the three methods. The method without density filter (solid line) is the worst one in terms of energy conservation and the method with Shepard filter (dashed line) the best one

propagation over a dry bed similar to the one analyzed in last subsection has been previously treated using SPH (Monaghan 1994, Colagrossi and Landrini 2003, Gómez-Gesteira and Dalrymple 2004, Violeau and Issa 2007, Crespo *et al.* 2007b) showing reasonable accuracy when compared with experiments. Nevertheless, considerably less attention has been paid to the study of dam break propagation over wet bed (Gómez-Gesteira and Dalrymple Crespo *et al.* 2008, Lee *et al.* 2008) where the complexity of fluid motion increases.

The laboratory experiments by Janosi *et al.* (2004) have been used to validate the dam break evolution over a wet bed simulated by SPH. This experiment is one of the validation test cases that can be found at the SPHERIC website (http://www.sphysics.org). The sketch of their experimental tank is shown in Fig. 12. The channel (right part of the sketch), begins at $x = 38$ cm and is 955 cm long and 15 cm wide. The bottom and side walls of the channel were constructed with glass. The lock

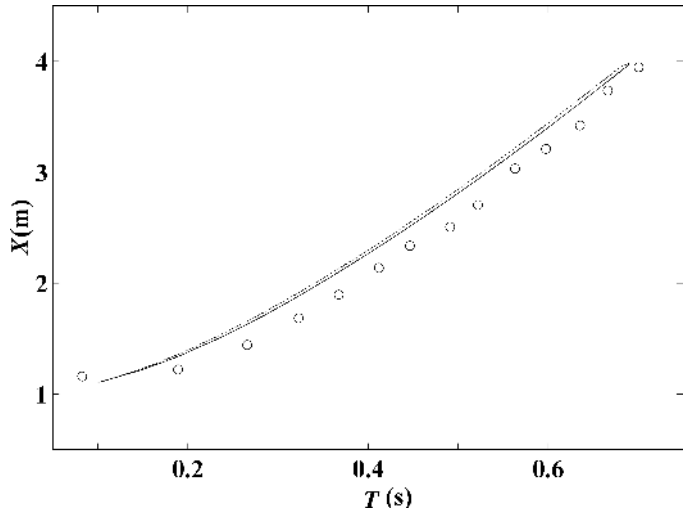

Figure 11 Dam break over a dry bed. Lines represent the X position of the dam toe for different numerical approaches. The solid line correspond to the case without kernel correction and the dashed one to the one with kernel gradient correction. Dots represent experimental data

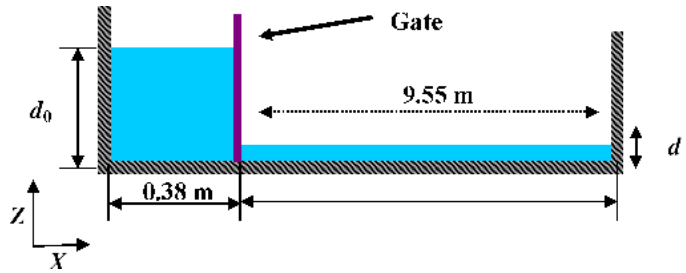

Figure 12 Setup of Janosi *et al.* (2004) experiment

(left part of the sketch) is 15 cm wide and 38 cm long including the lock gate. The lock was initially filled with water until $d_0 = 0.15$ m. The initial water depth in the channel, d, varied depending on the experiment. The experiments were recorded by two charge-coupled device cameras. Experimentally, the gate was removed from above at approximately constant velocity ($V_{\text{gate}} = 1.5\,\text{ms}^{-1}$).

Once again, the medium will be considered two-dimensional for computational purposes since the third dimension (the width) is negligible for the initial phenomenon under scope, namely the formation of multiply-connected shockwave which eventually breaks and overturns. Fluid particles were initially placed on a staggered grid with zero initial velocity. Nodes of the grid are located at $R = l\,dx\,\mathbf{i} + m\,dz\,\mathbf{k}$ with a two-point basis $(0, 0)$ and $(dx/2, dz/2)$ referred to the corner defined by R. l and m are integers, $\mathbf{i}, \mathbf{k}$ are unit vectors in X, Z directions, and $dx = dz = 0.005$ m. Fixed particles (bottom and walls) were placed in two rows forming a staggered grid with $dx = dz = 0.005$ m and zero initial velocity. Gate particles were initially placed in a single row with a finer interparticle spacing $(dx/2, dz/2)$ to prevent particle penetration. In most of SPH applications the gate separating both domains is instantaneously removed at the beginning of the calculation. However, experimentally it is known that the movement of the gate has been observed to play a key role in the early stages of the movement since its velocity was on the order

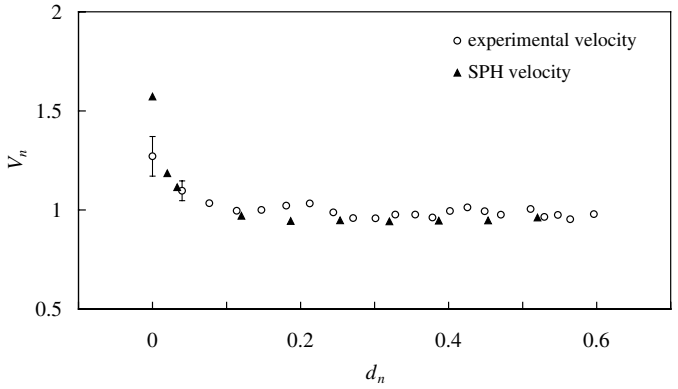

Figure 13 Comparison between experimental (dots) and numerical (triangles) dam-break velocity. Velocity was averaged in space during the first 3 m in both cases

of magnitude of water displacement. Numerically, the velocities and positions of the gate particles were externally imposed to mimic the experimental movement of the gate according to the constant velocities $V_x = 0.0\,\mathrm{ms}^{-1}$; $V_z = 1.5\,\mathrm{ms}^{-1}$.

The system was solved with a Verlet time–marching algorithm (Verlet 1967), using a cubic-spline kernel with smoothing length $h = 0.006$ m, dynamic boundary conditions (Crespo *et al.* 2007a), artificial viscosity, $\alpha = 0.08$ and the XSPH correction (Monaghan 1989) with $\varepsilon = 0.5$ to smooth gradients in fluid particles movement. The number of boundary particles was 3,879. The number of fluid particles depends on the water layer thickness, d, in the channel before the gate is lifted. According to Crespo *et al.* (2008), where a wide range of d values was considered, the number of fluid particles ranges from 4,484 for dam break movement on a dry bed to 30,884 with a water layer comparable to the initial dam break height, $d = 0.078$ m.

The capabilities of the SPH method to reproduce experimental results is shown in Fig. 13, were the numerical and experimental velocities of the leading edge are represented. Experimental and numerical velocities were spatially averaged along the first 3 m of the tank. Numerically, the position of the leading edge was calculated every 0.06 s and velocity was obtained by linear fitting. Both velocities and initial water depths are depicted in a dimensionless form. Velocity is normalized with $V = \sqrt{gd_0}$ and d/d_0 is the ratio between the initial water depth in the channel and lock region. The normalized velocity is observed to decrease with d. There is a good agreement between experimental measurements (light dots) and numerical results (dark squares) in most of the cases. Note that SPH velocity for a dry bed is higher than observed in the experiments, since experiments were not performed on a real dry bed, due to the impossibility of completely drying the tank.

An additional comparison between numerical and experimental results consists in calculating the free surface position. The experimental free surface was determined from digitized pictures (Janosi *et al.* 2004). Numerically, the free-surface level is evaluated by an iterative procedure that searches for any x coordinate the coordinate in z direction where the SPH particle density equals one half, although this definition may not be unique when the domain is not simply-connected as in the case of splashing or over-turning waves. The model is observed to reproduce the experimental profiles in Fig. 14. The case $d = 0.018$ was chosen to compare numerical results (solid) and experiments (dots). The water initially placed in the lock area pushes the channel water (first and second frames), generating the "mushroom" jet previously mentioned by Stansby *et al.* (1998) and Janosi *et al.* (2004). The first and second wave breaking can be observed in the third and sixth frames. Note that the shape of the front is completely different from the classical toe observed in dam break propagation over dry bed since the propagating water front in a completely dry dam break is a shallow water rarefaction wave (see for example the first and second snapshots in Fig. 2). Here, the leading edge is similar to that previously described in Gomez-Gesteira and Dalrymple (2004).

The observed difference between numerical and experimental results can be quantified by means of the two statistical parameters defined in Eq. (67), where now the variable under scope is the free-surface position. The good mean results obtained for $d = 0.018$ m ($A_r = 1.014$, $P_d = 0.076$) prove the accuracy of the method.

A variable that can also be obtained from SPH calculation is the vorticity, which can be calculated in lagrangian formalism following Monaghan (1992)

$$\omega_i = \sum_j m_j \frac{v_i - v_j}{\rho_i} \nabla_i W_{ij} \tag{70}$$

Different instants of dam break propagation can be observed in Figure 15 for $d = 0.018$ m where the color of each particle corresponds to its instantaneous vorticity. The water initially

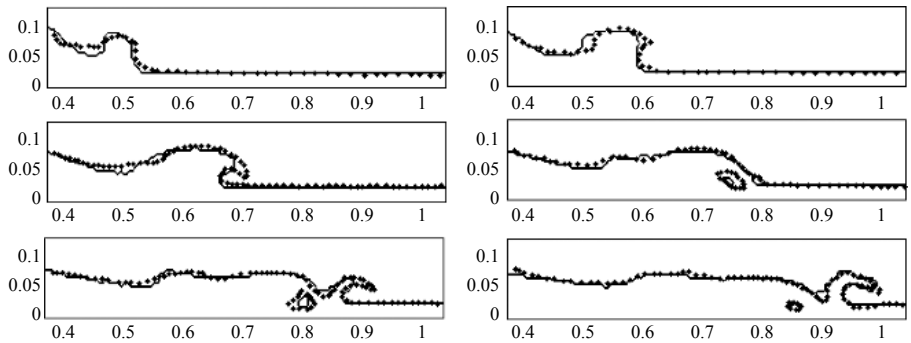

Figure 14 Comparison between experimental and numerical profiles of dam-break evolution over wet bed, ($d = 0.018$ m). Experimental values are represented by dots and numerical ones by solid lines

Figure 15 Vorticity plot for $d = 0.018$ m ($d/d_0 = 0.12$)

placed in the lock gate pushes the water initially placed in the channel ($t = 0.35$ s) giving rise to the "mushroom" jet mentioned above. Negative vorticity (light colors) appears on the left side of this "mushroom" due to counterclockwise water rotation. In addition, the frame also shows the beginning of the first wave breaking. The second frame ($t = 0.50$ s) corresponds to the instant previous to the second wave breaking. The figure also shows a positive eddy (dark color) generated after the first wave breaking. The third frame ($t = 0.65$ s), which generates the second positive eddy depicted in the fourth frame $t = 0.80$ s) shows a second eddy with positive vorticity (dark colors) generated by the second wave breaking. Positive vorticity near bed due to bottom friction can be observed in all frames, especially in the third and fourth ones. For a full description of the different breaking mechanisms depending on the initial water depth in the channel the reader is referred to Crespo *et al.* (2008).

5.4 *Collision between a 3D dam break and a structure*

The dam breaks considered in previous sections can be considered 2D. However, the nature of the observed phenomena becomes 3D when solid structures are hit by the incoming wave. Here we will examine the impact of a single wave with a tall structure. The resulting velocities and the force exerted by the wave on the structure are compared with experimental data taken by

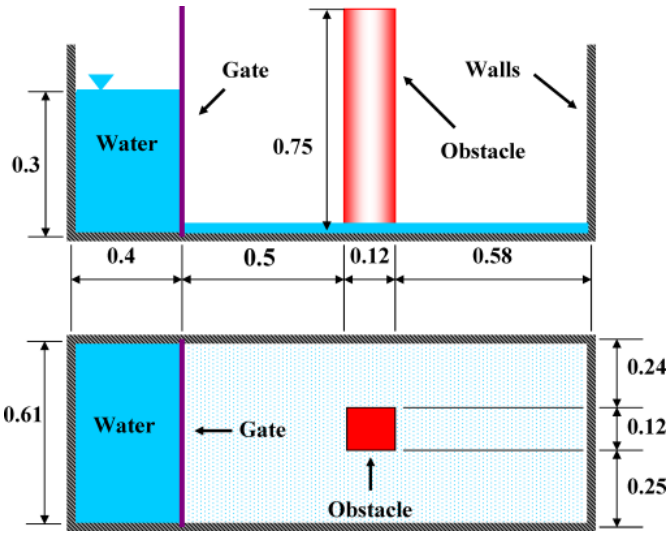

Figure 16 Experimental setup

Yeh and Petroff at the University of Washington. Previous comparisons to these data with a numerical model were carried out by P. Raad at Southern Methodist University, using his three dimensional Eulerian–Lagrangian marker and microcell (Chen *et al.* 1997), see http://engr.smu.edu/waves/solid.html for details about the experimental data. The same data were used by Gomez-Gesteira and Dalrymple (2004) to be compared with their SPH results.

The experimental domain (Fig. 16) is 160 cm long, 61 cm wide and 75 cm high. The volume of water initially contained behind the gate was 40 cm long × 61 cm wide × 30 cm high. The structure, which was 12 × 12 × 75 cm in size, was placed 50 cm downstream of the gate and 24 cm from the nearest sidewall of the tank. A thin water layer (approximately 1 cm deep) existed initially on the bottom of the tank, due to the experimental difficulty to completely drain the tank downstream of the gate prior to the dam break. Experimentally, the net force exerted on the structure and the fluid velocities at different locations were recorded. The velocity measurement was taken 14.6 cm upstream of the center of the structure and 2.6 cm off the floor of the tank.

The system was solved with a predictor-corrector algorithm (Monaghan 1989), using a cubic-spline kernel (Monaghan and Latanzio 1985) corrected following Bonet and Lok (1999) as described in Sec. 2.6.2.1 (see (24)). Dynamic boundary conditions (Crespo *et al.* 2007a), the XSPH correction (Monaghan 1989) with $\varepsilon = 0.5$ and a variable time step were also considered. Two different viscosity treatments were considered, artificial viscosity with $\alpha = 0.01$ and SPS viscosity (Eq. (56)). Fluid particles were initially placed on a staggered grid with zero initial velocity. Nodes of the grid are located at $R = l\,dx\,\mathbf{i} + m\,dx\,\mathbf{j} + m\,dz\,\mathbf{k}$ with a two-point basis (0,0) and $(dx/2, dy/2, dz/2)$ referred to the corner defined by R. l, m and n are integers, $\mathbf{i}$, $\mathbf{j}$, $\mathbf{k}$ are unit vectors in X, Y, Z directions. Fixed particles (bottom and walls) were placed in two rows forming a staggered grid with the same interspacing as the fluid particles. Both the initial spacing, dx, dy, dz, and the smoothing length, $h = 0.85\sqrt{dx^2 + dy^2 + dz^2}$, will depend on the different realizations of the numerical experiment. Figure 17 summarizes the number of particles (first panel) and the

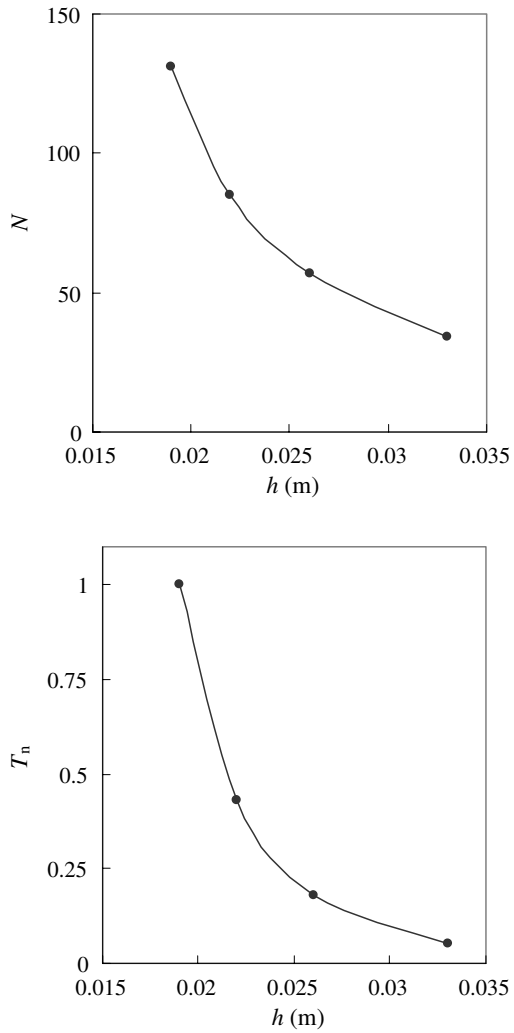

Figure 17 Dependence of the number of particles (N in the first panel) and normalized duration of the run (T_n in the second panel) on the smoothing length (h)

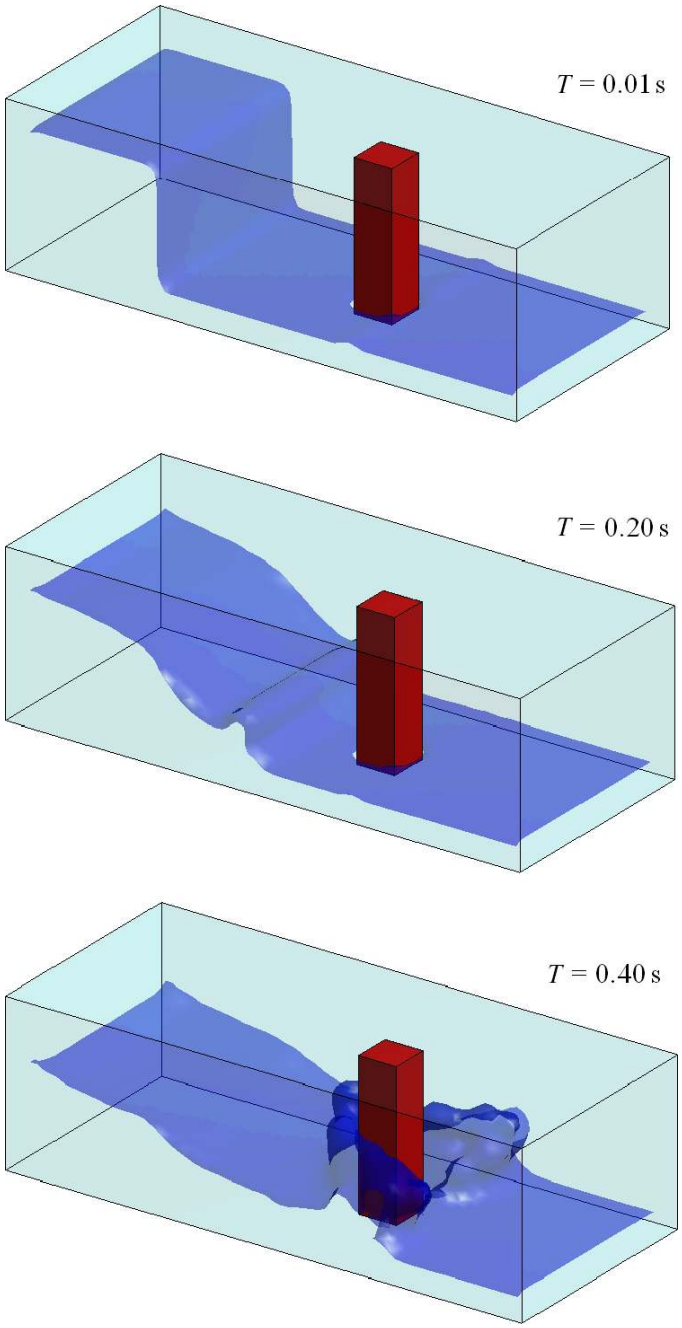

Figure 18 Different instants of dam break propagation over a wet bed. Initial movement of the dam break ($t = 0.01$ s). Dam break approaching the obstacle ($t = 0.20$ s). The shape of the leading edge depends on the presence of near bed water prior to the dam break arrival. Waveform hitting the structure ($t = 0.40$ s)

normalized duration (second panel) of the different realizations of the experiment. Note that a decrease in the smoothing length on the order of 50% results in an increase of the computational time on the order of 20 times.

Figure 18 shows different instants of wave propagation in collision with the structure. The initial movement of the dam break is shown at $t = 0.01$ s. At $t = 0.20$ s the dam break has advanced and approached the obstacle. Note that the water movement is completely 2D before the collision with the obstacle. The leading edge of this dam break is completely different from the one shown in Fig. 2. Instead of the typical toe observed over dry bed, it appears that the leading edge plows up the stationary water layer to create a waveform that would not be there in the absence of the water layer. This waveform is observed to hit the structure at $t = 0.40$ s. Thus, the experimental results are completely different from those that would occur if the bottom was dry beyond the gate as shown in (Gomez-Gesteira *et al.* 2004).

A preliminary comparison between the experimental and numerical results was carried out in previous studies (see Fig. 5 in Gomez-Gesteira *et al.* (2004)). Both the velocity (a) and the force (b) are observed to be accurately calculated, at least qualitatively, by the model. Here, a more detailed comparison will be considered. The original experimental series, which were not homogeneously sampled in time and some time multi-valued were interpolated by means of a spline function to obtain a new series at equally spaced, $\delta t = 0.015$ s, time intervals. This δt coincides with the recording period of the numerical signal in such a way that a point to point comparison can be performed between the experimental and numerical signals. The two parameters defined in Eq. (67), A_r and P_d, were considered, being velocity and force the variables of interest in this case. Figure 19 shows the relative amplitude (A_r) corresponding to velocity (first panel) and

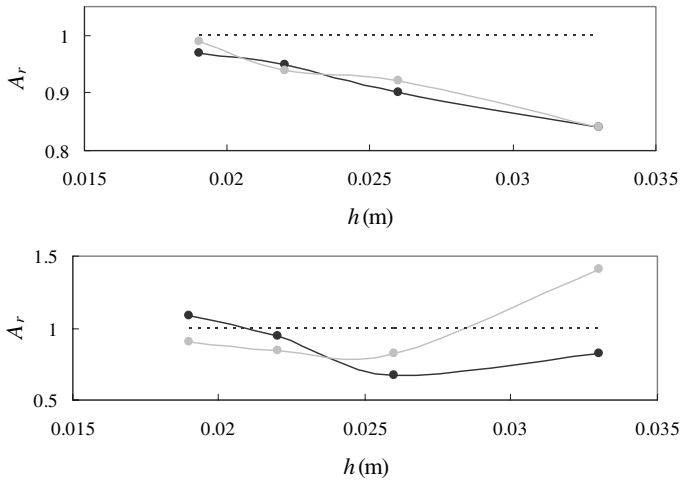

Figure 19 Relative amplitude (A_r) corresponding to velocity (first panel) and force (second panel). Dark solid lines correspond to calculations with artificial viscosity and light solid lines to SPS viscosity. The dashed line represents the theoretical perfect agreement between signals ($A_r = 1$)

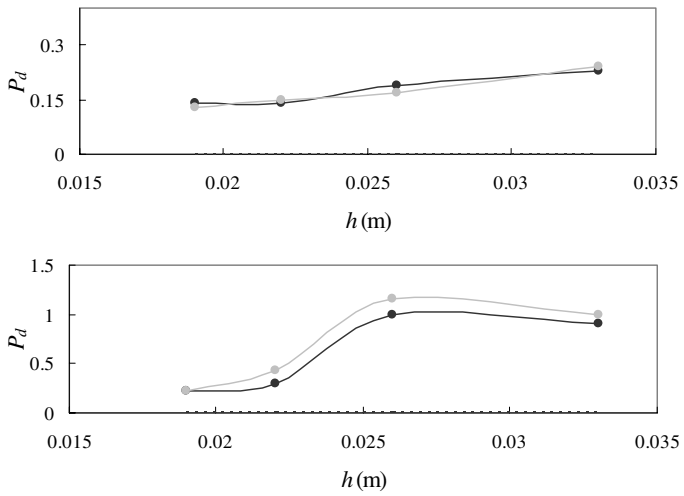

Figure 20 Phase difference (P_d) corresponding to velocity (first panel) and force (second panel). Lines as described in previous figure

force (second panel). Dark solid lines correspond to calculations with artificial viscosity and light solid lines to SPS viscosity. The dashed line represents the theoretical perfect agreement between signals ($A_r = 1$). Both for velocity and force, accuracy tends to increase when decreasing the smoothing length. Finally, both viscosity treatments provide similar results. Figure 20 shows the phase difference (P_d) corresponding to velocity (first panel) and force (second panel). Dark solid lines correspond to calculations with artificial viscosity and light solid lines to SPS viscosity. The dashed line represents the theoretical perfect agreement between signals ($P_d = 0$). Although velocity accuracy is good for any considered smoothing length, it increases when decreasing h. Force accuracy is not good when considering coarse resolutions, although it increases for smaller smoothing lengths. Once again, both viscosity treatments provide similar results which are not surprising as this case is dominated by gravity effects and an accurate modeling of turbulence is not essential for success here.

6 Conclusions

SPH has been shown to be a robust and powerful method for describing deforming media in a great variety of fields, for example, astrophysics, solid mechanics and fluid dynamics. In the particular case of computational fluid dynamics, the classical SPH formulation is especially well suited for problems involving large fluid deformation and fluid continuity breaking such as occur in highly nonlinear and potentially violent free-surface flows. Thus, problems like wave flooding and collision with obstacles can be handled in a natural way both in 2D and 3D.

One of the main drawbacks of the method is the need of a huge number of particles and very small time steps ($O(10^{-5}$ s)) to achieve high accuracy when compared with experimental results. This burden results in a high computational cost which can be partially alleviated by means of parallel (Moulinec *et al.* 2008, Maruzewsky *et al.* 2010, Lee *et al.* 2010) and GPU (Herault *et al.* 2010) computing. Both approaches will give rise to the main advances in applying the SPH technique during the next few years. An alternative way to speed up computations is to create hybrid methods, combining SPH with other techniques. Thus, Groenenboom and Cartwright (2010) combined SPH with a Finite Element model and Narayanaswamy *et al.* (2010) created a hybrid version of SPHysics and a wave propagation Boussinesq model.

Another limitation of the model is the formulation of an accurate viscosity treatment which will be particularly acute for problems at high Reynolds numbers, although important steps in the right direction have been given during the last decade (see Violeau and Issa (2007) for an overview), new research should be conducted to achieve robust and computationally efficient formulations.

An open question in SPH is the use of an equation of state to calculate pressure from density (slightly compressible approach) or to solve the Poisson equation (incompressible approach) to determine pressure. In spite of most of the authors have preferred the first approach (the one mainly used in this text), which results in an artificial decrease of the speed of sound, recently, some authors (Issa *et al.* 2005, Lee *et al.* 2008, Lee *et al.* 2010) have considered the incompressible approach with accurate results.

In summary, the considered 2D and 3D test cases have shown that the technique has reached a maturity that allows quantitative comparison with experimental measurements with an accuracy level similar to that observed for more conventional techniques.

Acknowledgments

This work was partially supported by Xunta de Galicia under project PGIDIT06PXIB383285PR. This work has also been supported by the U.K. Flood Risk Management Research Consortium II (FRMRC) and E.U. Marie Curie ToKIAP Project No.: 42350 (European SPH Initiative — ESPHI). RAD was partially supported by the Office of Naval Research, Coastal Geoscience Program.

Notation

$\mathbf{A}, \tilde{\mathbf{A}}$ = Matrices in MLS method
A = Scalar function
A_r = Relative Amplitude factor
$\mathbf{a}(\mathbf{x})$ = Coefficients of the interpolating function
B = Constant in the equation of state
c_0 = Speed of sound at the reference density
C = Constant in time-step control ($\sim$0.1)
C_I = Constant in SPS formalismo (0.0066)
C_s = Smagorinsky constant (0.12)
d = Initial water depth in the channel
d_0 = Initial water depth in the lock
dx, dy, dz = Inter-particle spacing
div = Divergence
e_i = Thermal energy of particle i
$f, \mathbf{f}$ = Scalar or vector variable used in kernel correction
e = Thermal energy
E = Energy
$\mathbf{g}$ = Gravitational acceleration
h = Smoothing length
$\mathbf{i}, \mathbf{j}, \mathbf{k}$ = Unit vectors
k = SPS turbulence kinetic energy
$\mathbf{L}$ = Matrix in corrected kernel gradient
$\mathbf{M}$ = Inverse of $\mathbf{L}$
m = Particle mass
M_d = Number of particles inside a domain
n = Integer in tensile instability correction (4)
$\mathbf{n}$ = Unit vector normal to the surface S and pointing upward
N = Number of particles
Num = Number of particles around particle i
$\mathbf{p}^{\mathrm{T}}(\mathbf{x})$ = Monomial
p = Pressure
P_d = Phase difference
$q_{\min}$ = Distance at which the first derivative of the kernel reaches a minimum
R_k = Coefficient in tensile instability correction
q = Normalized distance
R = Correlation coefficient
$\mathbf{s}$ = Position vector
S = Surface enclosing volume v
$S_{\mu\nu}$ = Element of SPS strain tensor
t = Time
$\mathbf{u}$ = Velocity vector
v = Volume of water
V = Coefficient for water velocity normalization ($\sqrt{gd_0}$)
$\mathrm{Var}^{\mathrm{exp}}$ = Experimental variable for statistical comparison
$\mathrm{Var}^{\mathrm{num}}$ = Numerical variable statistical comparison
V_{gate} = Gate velocity
V_x, V_z = Components of gate velocity
W_{ij} = Smoothing kernel in discrete notation (also $W(\mathbf{s}-\mathbf{x}_j, h)$)
$W(\mathbf{s}-\mathbf{x}_j, h)$ = Smoothing kernel in continuous notation
$\mathbf{x}$ = Position vector
x, y, z = Spatial coordinates
α = Coefficient in artificial laminar viscosity (0.5)
$\beta_0, \beta_{1x}, \beta_{1z}$ = Parameters in MLS method
γ = Coefficient in the equation of state (7)
δ = Dirac delta
δt = Sampling interval in 3D experiments (also recording period in numerics)
ΔE = Energy increment
Δl = Particle–particle spacing
Δt = Time-step
Δt_{cv} = Time-step control (based on Courant and viscosity terms)
Δt_f = Time-step control (based on force terms)
Δv_j = Volume associated to particle j
$\Delta\rho$ = Density increment due to fluctuation
ε = Parameter in XSPH correction (0.5)
ψ = Coefficient in tensile instability correction
η = Term in viscosity to prevent singularities ($= 0.1\,\mathrm{h}$)
ρ = Density
ρ_0 = Reference density
Π = Artificial viscosity term
$\tau_{\mu\nu}$ = Sub-particle stress tensor
υ_0 = Kinetic viscosity of laminar flow ($10^{-6}\,\mathrm{m^2 s^{-1}}$)
υ_t = Turbulence eddy viscosity
ω = Vorticity
∇ = Gradient
∇W = Kernel gradient
$\tilde{\nabla} W$ = Corrected kernel gradient

References

Batchelor, G.K. (1974). *Introduction to Fluid Dynamics*. Cambridge University Press, UK.

Berlytschko, T, Krongauz, Y., Organ, D., Fleming, M., Krysl, P. (1996). Meshless methods: an overview and recent developments. *Comput. Meth. Appl. Mech. Engrg.* 139, 3–47.

Belytschko, T., Krongauz, Y., Dolbow, J., Gerlach, C. (1998). On the completeness of meshfree particle methods. *Int. J. Numer. Mech. Engrg.* 43, 785–819.

Belytschko, T., Liu, W.K., Moran, B. (2000). *Nonlinear finite elements for continua and structures*. John Wiley and Sons.

Bonet J., Lok, T.-S.L. (1999). Variational and momentum preservation aspects of Smoothed Particle Hydrodynamic formulations. *Comput. Meth. Appl. Mech. Engrg.* 180, 97–115.

Capone, T., Panizzo, A., Cecioni, C., Dalrymple, R.A. (2007). Accuracy and stability of numerical schemes in SPH, in *Proc. of SPHERIC*, 156–160. eds. A.J.C. Crespo, M. Gómez-Gesteira, A. Souto-Iglesias, L. Delorme, J.M. Grassa.

Chanson, H. (2009). Application of the method of characteristics to the dam break wave problem. *J. Hydr. Res.* 47(1), 41–49 (DOI: 10.3826/jhr.2009.2865).

Chen, J.K., Beraun, J.E. (2000). A generalized smoothed particle hydrodynamics method for nonlinear dynamic problems. *Comput. Meth. Appl. Mech. Engrg.* 190, 225–239.

Chen, J. K., Beraun, J.E., Carney, T.C. (1999). A corrective Smoothed Particle Method for boundary value problems in heat conduction. *Comput. Meth. Appl. Mech. Engrg.* 46, 231–252.

Chen, S., Johnson, D.B., Raad, P.E., Fadda, D. (1997). The surface marker and microcell method. *Int. J. Numer. Meth. Fluids* 25, 749–778.

Colagrossi, A., Landrini, M. (2003). Numerical simulation of interfacial flows by smoothed particle hydrodynamics. *J. Comp. Phys.* 191, 448–475.

Cuomo, G., Panizzo, A., Dalrymple, R.A. (2006). SPH-LES two phase simulation of wave breaking and wave- structure interaction, in Proc. *30th Int. Conf. Coastal Engineering* (A.S.C.E.), 274–286.

Crespo, A.J.C., Gómez-Gesteira, M., Dalrymple, R.A. (2007a). Boundary conditions generated by dynamic particles in SPH methods. *CMC: Computers, Materials, & Continua* 5(3), 173–184.

Crespo, A.J.C., Gómez-Gesteira, M., Dalrymple, R.A. (2007b). 3D SPH Simulation of large waves mitigation with a dike. *J. Hydr. Res*. 45(5), 631–642.

Crespo, A.J.C., Gómez-Gesteira, M., Dalrymple, R.A. (2008). Modeling dam break behavior over a wet bed by a SPH technique. *J. Wtrwy. Port, Coastal and Ocean Engrg.* 134(6), 313–320. doi: 10.1061/(ASCE)0733-950X(2008) 134:6(313).

Dalrymple, R.A., Knio, O. (2001). SPH modelling of water waves. *Proc. Coastal Dynamics, Lund*, 779–787.

Dalrymple, R.A., Rogers, B.D. (2006). Numerical modeling of water waves with the SPH method, *Coastal Engrg*. 53(2–3), 141–147.

Dalrymple, R.A., Gómez-Gesteira, M., Rogers, B.D., Panizzo, A., Zou, S., Crespo, A.J.C., Cuomo, G., Narayanaswamy, M. (2009). Smoothed particle hydrodynamics for water waves, in *Advances in numerical simulation of nonlinear water waves*, ed. Ma, Q., World Scientific Publishing.

Delorme, L., Colagrossi, A., Souto-Iglesias, A., Zamora-Rodríguez, R., Botía-Vera, E. (2008). A set of canonical problems in sloshing, Part I: Pressure field in forced roll – comparison between experimental results and SPH. *Ocean Engrg*. (in press).

Dilts, G. (1999). Moving-least-square-particle hydrodynamics-I. consistency and stability. *Int. J. Numer. Meth. Engrg*. 44, 1115–1155.

Ferrari, A., Dumbser, M., Toro, E., Armanini, A. (2009). A new 3-D parallel SPH scheme for free surface flows, *Comput. Fluids* doi:10.1016/j.compfluid.2008.11.012.

Gingold, R. A., Monaghan, J.J. (1977). Smoothed particle hydrodynamics: Theory and application to non-spherical stars. *Mon. Not. R. Astron. Soc*. 181, 375–389.

Gómez-Gesteira, M. Dalrymple, R.A. (2004). Using a 3D SPH method for wave impact on a tall structure, *J. Wtrwy. Port, Coastal, Ocean Engrg*. 130(2), 63–69.

Gómez-Gesteira, M., Cerqueiro, D., Crespo, A.J.C., Dalrymple, R.A. (2005). Green water overtopping analyzed with an SPH model. *Ocean Engrg.* 32(2), 223–238.

Gómez-Gesteira M., Rogers, B.D., Dalrymple, R.A., Crespo, A.J.C., Narayanaswamy, M. (2009) *User Guide for the SPHysics code* (http://www.sphysics.org).

Gotoh, H., Shibihara, T., Hayashii, M. (2001). Subparticle-scale model for the mps method-lagrangian flow model for hydraulic engineering. *Comput. Fluid Dyn. J.* 9(4), 339–347.

Gotoh, H., Shao, S., Memita, T. (2004). SPH-LES model for numerical investigation of wave interaction with partially immersed breakwater. *Coastal Engrg. J.* 46(1), 39–63.

Groenenboom, P.H.L., Cartwright B.K. (2010). Hydrodynamics and fluid-structure interaction by coupled SPH-FE method. *J. Hydr. Res.* 48(Extra Issue), 61–73, doi:10.3826/jhr.2010.0004.

Hans, U.M. (1999). Review: Hydrocodes for structure response to underwater explosions. *Shock and Vibration* 6(2), 81–96.

Hérault, A., Bilotta, G., Dalrymple, R.A. (2010). SPH on GPU with CUDA. *J. Hydr. Res.* 48(Extra Issue), 74–79, doi: 10.3826/jhr.2010.0005.

Hieber S.E., Koumoutsakos P. (2008). An immersed boundary method for smoothed particle hydrodynamics of self-propelled swimmers, *J. Comp. Phys*. 227(19), 8636–8654.

Issa, R., Lee, E.-S., Violeau, D., Laurence, D.R. (2005). Incompressible separated flows simulation with the smoothed particle hydrodynamics gridless method. *Int. J. Numer. Meth. Fluids* 47, 1101–1106.

Janosi, I.M., Jan, D., Szabo, K.G., Tel, T. (2004). Turbulent drag reduction in dam-break flows. *Experiments in Fluids* 37, 219–229.

Johnson, G.R., Stryk, R.A., R., B.S. (1996). SPH for high velocity impact computations. *Comput. Meth. Appl. Mech. Engrg.* 139, 347–373.

Koshizuka, S. Tamako, H., Oka, Y. (1995). A particle method for incompressible viscous flow with fluid fragmentation. *Comput. Fluid Dyn. J.* 4, 29–46.

Koshizuka, S., Oka, Y. (1996). Moving-particle semi-implicit method for fragmentation of compressible fluid. *Nuclear Sci. Engrg.* 123, 421–434.

Kulasegaram, S., Bonet, J., Lewis R.W., Profit, M. (2004). A variational formulation based contact algorithm for rigid boundaries in two-dimensional SPH applications. *Comput. Mech.* 33(4), 316–325.

Landrini, M., Colagrossi, A., Greco, M., Tulin, M.P. (2007). Gridless simulations of splashing process and near-shore bore propagation. *J. Fluid Mech.* 591, 183–213.

Lee, E.-S., Moulinec, C., Xu, R., Violeau, D., Laurence, D., Stansby, P. (2008). Comparisons of weakly compressible and truly incomprensible algorithms for the SPH mesh free particle method. *J. Comput. Phys.* 227, 8417–8436.

Lee, E.-S., Violeau, D., Issa, R., Ploix, S. (2009). Application of weakly compressible and truly incompressible SPH to 3-D water collapse in waterworks. *J. Hydr. Res.* 48(Extra Issue), 50–60, doi:10.3826/jhr.2010.0003.

Libersky, L.D., Petschek, A.G., Carny, T.C., Hipp, J.R., Allahdady, F.A. (1993). High strain Lagrangian hydrodynamics a three-dimensional (SPH) code for dynamic material response. *J. Comput. Phys.* 109, 67–75.

Liu, P.L.F., Losada, I.J. (2002). Wave propagation modeling in coastal engineering. *J. Hydr. Res.* 40(3), 229–240.

Liu, G.R. (2003). *Meshfree Methods: Moving Beyond Finite Element Method*, CRC Press.

Liu, G., Liu, M. (2003). *Smoothed Particle Hydrodynamics: A Meshfree Particle Method*, World Scientific.

Liu, W., Li, S., Belytscho, T. (1997). Moving least square Kernel Galerkin method (I) methodology and convergence. *Comput. Meth. Appl. Mech. Engrg.* 143, 113.

Lucy, L. (1977). A numerical approach to the testing of fusion process. *J. Astronomical* 82, 1013–1024.

Marongiu, J.C., Leboeu, F., Parkinson, E. (2007). Numerical simulation of the flow in a Pelton turbina using the meshless method smoothed particle hydrodynamics: A new simple solid boundary treatment. Proc. *IMechE*, 221 (Part A), *J. Power and Energy*. doi: 10.1243/09576509JPE465.

Maruzewski, P., Le Touzé, D., Oger, G., Avellan, F. (2010). SPH high-performance computing simulations of rigid solids impacting the free-surface of water. *J. Hydr. Res.* 48(Extra Issue), 126–134.

Molteni, D., Colagrossi, A., Colicchio, G. (2007). On the use of an alternative water state equation for SPH. Proc. of *SPHERIC*, 156–160. eds. A.J.C. Crespo, M. Gómez-Gesteira, A. Souto-Iglesias, L. Delorme, J.M. Grassa.

Monaghan, J.J. (1982). Why particle methods work? *SIAM J. Scientific and Statistical Comput*. 3(4), 422–433.

Monaghan, J.J. (1989). On the problem of penetration in particle methods. *J. Comp. Phys.* 82, 1–15.

Monaghan, J.J. (1992). Smoothed particle hydrodynamics. *Ann. Rev. Astron. Appl.* 30, 543–574.

Monaghan, J.J. (1994). Simulating free surface flows with SPH. *J. Comput. Phys.* 110, 399–406.

Monaghan, J.J. (1996). Gravity currents and solitary waves. *Phys. D* 98, 523–533.

Monaghan, J.J. (1997). Implicit SPH drag and dust dynamics. *J. Comput. Phys.* 138, 801–820.

Monaghan, J.J. (2000). SPH without a tensile instability. *J. Comput. Phys.* 159, 290–311. doi:10.1006/jcph.2000.6439.

Monaghan, J.J. (2005). Smoothed particle hydrodynamics. *Rep. Prog. Phys*. 68, 1703–1759. doi:10.1088/0034-4885/68/8/R01.

Monaghan, J.J., Cas, R.A.F., Kos, A.M., Hallworth, M. (1999). Gravity currents descending a ramp in a stratified tank. *J. Fluid Mech.* 379, 39–70.

Monaghan, J.J., Kos, A. (1999). Solitary waves on a Cretan beach. *J. Wtrwy. Port, Coastal Engrg.* 125(3), 145–154.

Monaghan, J.J., Kos, A. (2000). Scott Russell's wave generator. *Phys. Fluids* 12(3), 622–630.

Monaghan, J.J., Lattanzio, J.C. (1985). A refined method for astrophysical problems. *Astron. Astrophys.* 149, 135–143.

Morris, J.P., Fox, P.J., Shu, Y. (1997). Modeling lower Reynolds number incompressible flows using SPH. *J. Comput. Phys.* 136, 214–226.

Moulinec, C., Issa, R., Marongiu, J.C., Violeau, D. (2008). Parallel 3-D SPH simulations. *Comput. Model. Eng. Sci.* 25(3), 133–148.

Narayanaswamy, M.S., Crespo, A.J.C., Gómez-Gesteira, M., Dalrymple, R.A. (2010) SPHysics-FUNWAVE hybrid hodel for coastal wave propagation. *J. Hydr. Res.*, 48(Extra Issue), 85–93. doi:10.3826/jhr.2010.0007.

Nsom, B., Debiane, K., Piau, J.M. (2000). Bed slope effect on the dam break problem. *J. Hydr. Res.* 38(6), 459–464.

Oger, G., Doring, M., Alessandrini, B., Ferrant P. (2006). Two-dimensional SPH simulations of wedge water entries. *J. Comput. Phys.* 213(2), 803–822.

Oger, G., Doring, M., Alessandrini, B., Ferrant P. (2007). An improved SPH method: Towards higher order convergence. *J. Comput. Phys.* 225, 1472–1492.

Peskin, C.S. (1977). Numerical analysis of blood flow in the heart. *J. Comput. Phys.* 25, 220–252.

Randles, P.W., Libersky, L.D. (1996). Smoothed particle hydrodynamics: Some recent improvements and applications. *Comput. Meth. Appl. Mech. Engrg.* 138, 375–408.

Rogers, B.D., Dalrymple, R.A. (2008). SPH Modeling of tsunami waves, *Advances in Coastal and Ocean Engineering,* 10*, Advanced Numerical Models for Tsunami Waves and Runup*, World Scientific.

Shao, S.D. (2005). SPH simulation of solitary wave interaction with a curtain-type breakwater. *J. Hydr. Res.* 43(4), 366–375.

Shao, S. D. (2006). Simulation of breaking wave by SPH method coupled with K-Epsilon model, *J. Hyd. Res.* 44(3), 338–349.

Shao, S. D., Gotoh, H. (2005). Turbulence particle models for tracking free surfaces, *J. Hyd. Res.* 43(3), 276–289.

Shao, S.D., Lo, E.Y.M. (2003). Incompressible SPH method for simulating Newtonian and non-newtonian flows with free surface. *Adv. Water Resour*. 26(7), 287–800.

Smagorinsky, J. (1963). General circulation experiments with the primitive equations: I. The basic Experiment. *Monthly Weather Review* 91, 99–164.

Souto-Iglesias, A., Pérez Rojas, L., Zamora Rodríguez, R. (2004). Simulation of anti-roll tanks and sloshing type problems with smoothed particle hydrodynamics. *Ocean Engrg.* 31, 1169–1192.

Souto-Iglesias, A, Delorme, L., Pérez Rojas, L., Abril, S. (2006). Liquid moment amplitude assessment in sloshing type problems with SPH. *Ocean Engrg.* 33, 11–12.

Stansby, P.K., Chegini, A., Barnes, T.C. (1998). The initial stages of dambreak flow. *J. Fluid Mech.* 374, 407–424.

Vaughan, G.L., Healy, T.R., Bryan, K.R., Sneyd, A.D., Gorman, R.M. (2008). Completeness, conservation and error in SPH for fluids, *Int. J. Num. Meth. Fluids* 56, 37–62.

Verlet, L. (1967). Computer experiments on classical fluids. I. Thermodynamical properties of Lennard-Jones molecules. *Phys. Rev*. 159, 98–103.

Viccione, G. Bovolin, V., Carratelli, E.P. (2008). Defining and optimizing algorithms for neighbouring particle identification in SPH fluid simulations. *Int. J. Numer. Meth. Fluids* 58, 625–638. doi: 10.1002/fld.1761.

Vila, J.P. (1999). On particle weighted methods and SPH. *Math. Models Meth. Appl. Sci.* 9, 161–210.

Violeau, D., Issa, R. (2007). Numerical modelling of complex turbulent free surface flows with the SPH method: An overview. *Int. J. Numer. Meth. Fluids* 53(2), 277–304.

Wendland, H. (1995). Piecewiese polynomial, positive definite and compactly supported radial functions of minimal degree. *Advanc. Comput. Math.* 4(1), 389–396.